Article

MMS

Mathematics and Mechanics of Solids
2023, Vol. 28(3) 748–772

DOI: 10.1177/10812865221094833
journals.sagepub.com/home/mms
SAGE

Understanding the role of interfacial mechanics on the wrinkling behavior of compressible bilayer structures under large plane deformations

A Derya Bakiler
Department of Mechanical Engineering, Bilkent University, Ankara, Turkey

Ali Javili
Department of Mechanical Engineering, Bilkent University, Ankara, Turkey

Received 26 January 2022; accepted 28 March 2022

Abstract

Layered soft structures under loading may buckle in order to release energy. One commonly studied phenomenon is the wrinkling behavior of a bilayer system consisting of a stiff film on top of a compliant substrate, which has been observed ubiquitously in nature and has found several applications. While the wrinkling behavior of the *incompressible* bilayer system has been explored thoroughly, the large deformation behavior of a *compressible* bilayer system had been virtually unexplored until very recently. On the contrary, it is well established where more than one material is concerned, there always exists an interphase region between different constituents whose mechanical modeling has presented itself as a long-lasting challenge. To address these gaps in the literature, herein we first propose a theoretical, generic, large deformations framework to capture the instabilities of a compressible domain containing an interface. The general interface model is employed such that at its limits, the elastic and the cohesive interface models are recovered. The instability behavior of a compressible bilayer domain undergoing large deformations for a wide range of cohesive stiffness values, stiffness ratios, compressibilities, and film thicknesses is systematically explored. In particular, it is shown that delamination of the film can also be captured via this interface model. In addition, this generic framework is examined for a coated beam and a coated half-space too. The results of the theoretical framework are thoroughly compared to numerical results obtained via finite element method simulations enhanced with eigenvalue analysis, and an excellent agreement between the two sets of results is observed. It is found that varying substrate Poisson's ratio has a significant effect on the bifurcation behavior for higher cohesive stiffnesses. Remarkably, while in classical bilayers the critical stretch at wrinkling is independent of the film thickness, herein we discover a significant dependence of the critical stretch to the film thickness in the presence of the interface.

Keywords

Instabilities, bilayer wrinkling, compressibility, general interface model

Corresponding author:
Ali Javili, Department of Mechanical Engineering, Bilkent University, Rektorluk, EA 132, 06800 Ankara, Turkey.
Email: ajavili@bilkent.edu.tr

1. Introduction

The bilayer structure has been of increasing interest due to its myriad of applications and occurrences in nature, especially for bio-mechanical instabilities as observed in the brain [1] and airways [2]. However, where more than one material is concerned, such as in the case of a bilayer, there always exists an interphase layer between the two materials, which plays a key role in the overall response of the structure. Until now, this interphase layer in bilayer structures has been commonly neglected by assuming perfect bonding between the layers [3]. Alternatively, in very few contributions, the interphase effect has been treated as a layer of its own resulting in a trilayer structure [4], or it has been modeled via a cohesive interface model [5]. The cohesive interface model, however, is only one limit of the *general interface model* [6]. To our knowledge, the general interface model has not yet been incorporated into bilayer instabilities. On the contrary, even with the cohesive interface layer, the available studies in literature are limited to incompressible bilayers only. Thus, the main objectives of this work are as follows: (a) to introduce the general interface model to a bilayer structure consisting of a film and a substrate, and (b) to perform an incremental instability analysis on the former in large deformations setting for *compressible* material behavior. Furthermore, throughout the illustrative examples, the results of the developed theoretical model are compared with the numerical results of our in-house finite element code enhanced with eigenvalue analysis.

Instabilities of layered systems are observed ubiquitously in nature, such as in the brain [7], skin [8], and airways [2], while also being harnessed in several applications such as buckling-based metrology [9], sensors [10], and stretchable electronics [11]. Following the pioneering works of Biot [12,13] and Allen [14], understanding, and in turn harnessing, the instabilities of such systems has been subject to prolific growth. Layered systems have often been approximated as bilayer systems, which consist of a thin layer or film on top of a usually more compliant, thicker substrate. The bilayer system itself has many different parameters which influence its bifurcation behavior, such as the nature of loading [15], for example, prestretch [3,16] or growth [17,18], imperfections [19], curvature [20], and substrate nonlinearity [21]. Works have also been conducted on different geometries of bilayers, including cylindrical tubes [22] and shells [23,24], and on postbifurcation modes [25]. The large deformation analysis of the effect of compressibility on bifurcation behavior remains yet widely unexplored, as most works assume incompressibility from the onset. The compressible half-space has been investigated in previous studies [26–28], followed by the compressible bilayer [29].

When two materials are bonded at an interface, unlike what is assumed in the great majority of the works on bilayer structures thus far, the bonding is subject to various imperfections, hence creating an interphase layer between the two [30]. Stafford et al. [4] accounted for this interphase layer, motivated by the different properties a film on a substrate displays along its depth, and have paved the way for many contributions on trilayer systems [9,31–35], also finding applications serving as an adhesive layer [36] or for strain isolation [37]. Bifurcation of elastic solids with sliding interfaces has been recently investigated by Bigoni et al. [38].

Another way to capture the behavior of the interphase layer is to introduce a zero-thickness interface model in place of the interphase layer [39,40]. This zero-thickness interface model, for mechanical problems, is classified based on the continuity of the displacement and traction fields across this interface, and how these fields relate to interphase properties [41–43]. Incorporating an interface into the bilayer structure is crucial, as, for instance, allowing for displacement discontinuity across the interphase allows for the phenomenon such as delamination [44] to be captured. Even though there are some applications in which delamination is an undesired by-product of the manufacturing process [45,46], understanding, and in turn harnessing, delamination behavior [47] has become a crucial aspect of flexible electronics [48,49] and novel surface renewal mechanisms [50]. Figure 1 outlines schematically the four categories under which interface models can be grouped depending on the continuity of these fields, briefly reviewed below. For further details on the analytical and computational aspects of the works done on each model, applications of interfaces in composites, and extensions to more sophisticated interface models, see Firooz et al. [30].

- *The perfect interface model* refers to the trivial interfaces in which both the displacement and traction are continuous across the interface, and is also referred to as free singular surfaces [51]. Since this assumption of continuity in both fields is the most elementary one, it is referred to as the

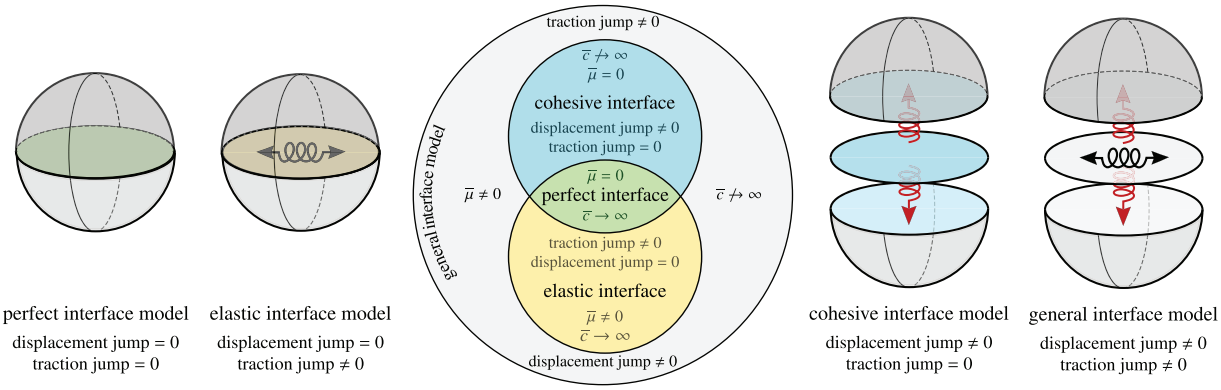

Figure 1. The four groups of interface models categorized by field jump conditions, namely, as the perfect, elastic, cohesive, and general interface models, where $\bar{\mu}$ is a surface elasticity parameter and $\bar{c}$ is the cohesive stiffness parameter.

"perfect model," and all other subsequent models with discontinuities are thus referred to as "imperfect models."

- *The cohesive (spring-type) interface model* is a type of imperfect interface model in which displacement jumps are allowed for, but the traction across the interface is assumed to be continuous. The seminal works on the topic include those of Barenblatt [52,53] and Dugdale [54], while the model has found applications in peeling [55], delamination [56–58], debonding [59], fracture [60,61], and crack growth [62–65], along with computational implementations [66,67].
- *The elastic (stress-type) interface model* allows for a traction jump across the interface, while assuming that the displacement field remains continuous. Also identified as thermodynamic singular surfaces [51], the traction jump across this interface model is a result of the tension along the interface together with the curvature and relates to the generalized Young–Laplace equation [68,69], and has roots in the surface elasticity theory of Gurtin and Murdoch [70]. Interface elasticity theory [71,72] has been further extended in previous studies [73,74] among others.
- *The general interface model* combines the cohesive and elastic interface models, allowing for both jumps in the displacement and traction fields. Contrary to the previous models, this model is more recent and has been studied in a few works, for instance, in previous works [42,75–78], and further extended in the work of Firooz et al. [30]. While the cohesive interface model is formulated as the asymptotic limit of a thin "soft" interphase, and the elastic interface model as the limit of a thin "stiff" interphase, the general interface model encompasses the whole range. The formulation of generalized interfaces in a variationally consistent manner for finite deformations [6] will serve as the basis of the interface analysis in this work.

1.1. Notation and definitions

Interface quantities denoted as $\{\overline{\bullet}\}$ are distinguished from their bulk counterparts denoted as $\{\bullet\}$. The superscript $\{\bullet\}^+$ denotes a quantity on the plus side of the interface, while $\{\bullet\}^-$ denotes the minus side. The unit normal to the interface points from the minus side to the plus side of the interface. The jump of a quantity across the interface is defined by $[[\{\bullet\}]] := \{\bullet\}^+ - \{\bullet\}^-$, whereas the average of a quantity is defined by $\{\{\{\bullet\}\}\} := \frac{1}{2}[\{\bullet\}^+ + \{\bullet\}^-]$. Since one of the main objectives of this work is to introduce the general interface model into a bilayer structure composed of a film and substrate, the plus side and all parameters associated with it will be denoted as the "film," hence with the subscript $\{\bullet\}_f$, while the minus side is referred to as the "substrate" denoted as $\{\bullet\}_s$. The contraction of two second-order tensors $\boldsymbol{A}$ and $\boldsymbol{B}$ is denoted as $\boldsymbol{A} : \boldsymbol{B} = A_{ij}B_{ij}$, while $[\boldsymbol{A} \cdot \boldsymbol{B}]_{ij} = A_{is}B_{sj}$. Fourth-order constitutive tensors are written with a different font, such as $\mathbb{I}$ denoting the fourth-order identity tensor. The tensor product of two second-order tensors $\boldsymbol{A}$ and $\boldsymbol{B}$ is a fourth-order tensor $\mathbb{D} = \boldsymbol{A} \otimes \boldsymbol{B}$ with $D_{ijkl} = A_{ij}B_{kl}$. Two

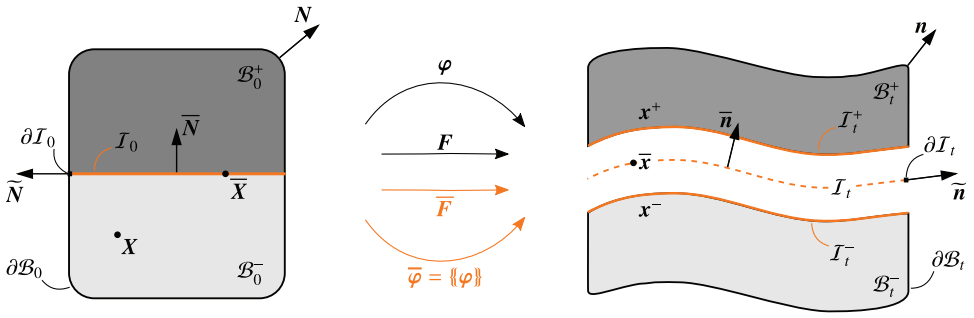

Figure 2. The deformation of a continuum body which occupies the material configuration $\mathcal{B}_0 \subset \mathbb{R}^3$ at time $t = 0$ that is mapped to the spatial configuration $\mathcal{B}_t \subset \mathbb{R}^3$ at any time $t > 0$ via the nonlinear deformation map $\boldsymbol{\varphi}$. The two sides of the body in the material configuration intersect at the interface $\mathcal{I}_0$. The interface is a zero-thickness layer that divides the bulk into the two parts $\mathcal{B}_0^-$ and $\mathcal{B}_0^+$ initially with $[[\boldsymbol{X}]] = \boldsymbol{0}$, which through the mapping $\boldsymbol{\varphi}$ opens up, creating a displacement jump across the interface such that $[[\boldsymbol{x}]] \neq \boldsymbol{0}$ is allowed for.

nonstandard tensor products of two second-order tensors $\boldsymbol{A}$ and $\boldsymbol{B}$ are defined as $[\boldsymbol{A} \,\overline{\otimes}\, \boldsymbol{B}]_{ijkl} := A_{ik} B_{jl}$ and $[\boldsymbol{A} \,\underline{\otimes}\, \boldsymbol{B}]_{ijkl} := A_{il} B_{jk}$.

1.2. Organization of the manuscript

The remainder of the manuscript is organized as follows. Section 2 briefly summarizes the unifying approach for compressible domains, while extending it to incorporate the general interface model. Next, the developed generic framework is applied to analyze the bifurcation behavior of a coated half-space in Section 3 and a coated beam in Section 4. The developed framework is applied to a bilayer domain consisting of a film and substrate in Section 5, wherein the two layers are attached by a general interface, and the results of the theoretical derivations are compared with those of numerical simulations obtained via our own in-house computational code using the finite element method (FEM) enhanced with eigenvalue analysis. Section 6 concludes this work and provides further outlook.

2. Generic compressible domain with interface instability formulation

This work extends the unifying framework toward geometric instabilities of compressible domains under plane compression developed in Bakiler et al. [29] accounting for the general interface model. This section briefly summarizes the approach and its adaptation to include interface quantities, while also introducing the notation. The developed framework here is then applied to the specific geometries of half-space, beam, and bilayer in the upcoming sections. For the half-space and beam geometries, the interface reduces to coating associated with the surface elasticity theory.

The material and spatial configurations of a continuum body with an interface are depicted in Figure 2 showing a continuum body that initially takes the material configuration $\mathcal{B}_0 \subset \mathbb{R}^3$ at time $t = 0$ with $\boldsymbol{X}$ denoting the reference placement of particles of the bulk in this configuration. The bulk of the material configuration is mapped to its spatial configuration $\mathcal{B}_t \subset \mathbb{R}^3$ at a time t via the nonlinear deformation map $\boldsymbol{\varphi}$ according to $\boldsymbol{x} = \boldsymbol{\varphi}(\boldsymbol{X}, t)$ with $\boldsymbol{x}$ denoting the current placement of particles in the spatial configuration. The particles on the interface are mapped from their material configuration $\mathcal{I}_0$ to their spatial configuration $\mathcal{I}_t$ through the mapping:

$$\bar{\boldsymbol{x}} = \bar{\boldsymbol{\varphi}}(\bar{\boldsymbol{X}}, t), \quad \text{where} \quad \bar{\boldsymbol{\varphi}} = \{\!\{\boldsymbol{\varphi}\}\!\}. \tag{1}$$

The projection of the identity tensor $\boldsymbol{I}$ onto the interface renders the interface identity tensor $\overline{\boldsymbol{I}} = \boldsymbol{I} - \overline{\boldsymbol{N}} \otimes \overline{\boldsymbol{N}}$, where $\overline{\boldsymbol{N}}$ is the unit normal to the interface in the material configuration, pointing from the minus side to the plus side of the interface, whereas $\bar{\boldsymbol{n}}$ denotes its spatial counterpart. The deformation gradient for material points in the bulk is defined as $\boldsymbol{F} := \operatorname{Grad} \boldsymbol{\varphi}$ and maps the material line element $d\boldsymbol{X}$ to its spatial counterpart $d\boldsymbol{x}$ such that $d\boldsymbol{x} = \boldsymbol{F} \cdot d\boldsymbol{X}$, while the Jacobian refers to $J := \operatorname{Det} \boldsymbol{F}$. The interfacial counterpart of deformation gradient, $\bar{\boldsymbol{F}}$, can be obtained by projecting $\operatorname{Grad} \bar{\boldsymbol{\varphi}}$ onto the

interface, that is, $\bar{\boldsymbol{F}} = \mathrm{Grad}\,\bar{\boldsymbol{\varphi}} \cdot \bar{\boldsymbol{I}}$, which can also be expressed via relation (1) as $\bar{\boldsymbol{F}} = \mathrm{Grad}\,(\{\{\boldsymbol{\varphi}\}\}) \cdot \bar{\boldsymbol{I}} = \{\{\mathrm{Grad}(\boldsymbol{\varphi})\}\} \cdot \bar{\boldsymbol{I}} = \{\{\boldsymbol{F}\}\} \cdot \bar{\boldsymbol{I}}$. For the problem at hand, for a uniaxial tension/compression under plane-strain constraints, the deformation gradient reads $\boldsymbol{F} = \mathrm{Diag}(\lambda, \eta, 1)$, with λ and η being the horizontal and vertical stretches, and its interfacial counterpart can be constructed via $\bar{\boldsymbol{F}} = \boldsymbol{F} \cdot \bar{\boldsymbol{I}}$, since both parts of the domain undergo the same applied stretch $\lambda = \lambda_f = \lambda_s$. In the absence of body forces, quasi-static large deformation continuum mechanics is governed by the fundamental equilibrium equation:

$$\mathrm{Div}\,\boldsymbol{P} = \boldsymbol{0} \quad \text{in } \mathcal{B}_0, \tag{2}$$

in which $\boldsymbol{P}$ denotes the Piola stress. On the contrary, in the absence of interface force densities, the interface balance equations [6] read:

$$\overline{\mathrm{Div}}\,\overline{\boldsymbol{P}} + [[\boldsymbol{P}]] \cdot \overline{\boldsymbol{N}} = \boldsymbol{0} \;\text{ on }\; \mathcal{I}_0\,(\text{along}) \;\text{ and }\; \bar{\boldsymbol{t}} - \{\{\boldsymbol{P}\}\} \cdot \overline{\boldsymbol{N}} = \boldsymbol{0} \;\text{ on }\; \mathcal{I}_0\,(\text{across}). \tag{3}$$

It should be noted that in the case where the stress along the interface $\overline{\boldsymbol{P}} = \boldsymbol{0}$, the balance equation (3) reduces to $[[\boldsymbol{P}]] \cdot \overline{\boldsymbol{N}} = \boldsymbol{0}$, which can also be written as the sum of tractions across the interface set to zero, ensuring traction continuity, that is, $\sum \boldsymbol{P} \cdot \boldsymbol{N} = \boldsymbol{0}$.

Constitutive models for material behavior are commonly based on a phenomenological free energy density [79]. Herein, the material behavior is assumed to be isotropic and homogeneous, and therefore the hyperelastic free energy per volume in the material configuration ψ remains a function of the deformation gradient $\boldsymbol{F}$ only. A compressible material model is employed throughout this work; this implies that the Poisson's ratio ν also governs the material's behavior. The plane-strain definition of Poisson's ratio will be used herein, such that, excluding the auxetic regime, $0 \leqslant \nu < 1$, where $\nu = 0$ indicates full compressibility and $\nu \to 1$ indicates incompressibility. This plane-strain definition relates to its three-dimensional (3D) counterpart such that $\nu_{3\mathrm{D}} = \frac{\nu}{1+\nu}$. The behavior of the hyperelastic domain here will be modeled via a compressible neo-Hookean model [79] with the polyconvex free energy density:

$$\psi(\boldsymbol{F}) = \tfrac{1}{2}\mu[\boldsymbol{F} : \boldsymbol{F} - 3 - 2\ln J] + 2\mu\alpha\left[\tfrac{1}{4}\left[J^2 - 1\right] - \tfrac{1}{2}\ln J\right], \;\text{ where }\; \alpha = \frac{\nu}{1-\nu}. \tag{4}$$

The coefficient μ is the *second Lamé parameter*, and the coefficient $2\mu\alpha$ is the *first Lamé parameter* written in an alternate format by defining the penalty parameter α for compressibility that ranges from full compressibility at $\alpha = 0$ to incompressibility at $\alpha \to \infty$. The interface counterpart of the free energy density $\bar{\psi}$ as a function of interface deformation gradient $\bar{\boldsymbol{F}}$ and interface displacement jump $\bar{\boldsymbol{f}} := [[\boldsymbol{x}]]$ is

$$\bar{\psi}(\bar{\boldsymbol{F}}, \bar{\boldsymbol{f}}) = \tfrac{1}{2}\overline{\mu}\,[\bar{\boldsymbol{F}} : \bar{\boldsymbol{F}} - 2 - 2\ln \bar{J}] + \tfrac{1}{2}\overline{\Lambda}[\tfrac{1}{2}[\bar{J}^2 - 1] - \ln \bar{J}] + \tfrac{1}{2}\bar{c}\bar{\boldsymbol{f}} \cdot \bar{\boldsymbol{f}} \;\text{ with }\; \bar{J} := \overline{\mathrm{Det}}\bar{\boldsymbol{F}}, \tag{5}$$

where $\bar{\mu}$ and $\overline{\Lambda}$ are interface material parameters, which correspond to the in-plane interface response. Both $\bar{\mu}$ and $\overline{\Lambda}$ can be referred to as interface Lamé parameters, with units of N/m. The parameter $\bar{c}$ is indicative of the resistance of the interface to opening, hence relating to the orthogonal stiffness of the interface, having the unit of $\mathrm{N/m^3}$. For the following formulations, we set $\overline{\Lambda} = 0$ without loss of generality and work only with $\bar{\mu}$, since in the two-dimensional (2D) setting here both of these parameters serve the same purpose of relating to the resistance of the interface to a change in length along the interface. Clearly, the perfect interface model is recovered when $\bar{\mu} \to 0$ and $\bar{c} \to \infty$. The Piola stress that derives from the free energy (equation (4)) reads:

$$\boldsymbol{P} := \frac{\partial \psi}{\partial \boldsymbol{F}} = \mu\left[\boldsymbol{F} - \boldsymbol{F}^{-t}\right] + \mu\alpha\left[J^2 - 1\right]\boldsymbol{F}^{-t}, \tag{6}$$

whereas its interfacial counterparts are

$$\bar{\boldsymbol{P}} := \frac{\partial \bar{\psi}}{\partial \bar{\boldsymbol{F}}} = \bar{\mu}[\bar{\boldsymbol{F}} - \bar{\boldsymbol{F}}^{-\mathrm{t}}] \;\text{ and }\; \bar{\boldsymbol{t}} := \frac{\partial \bar{\psi}}{\partial \bar{\boldsymbol{f}}} = \bar{c}\bar{\boldsymbol{f}}. \tag{7}$$

We now proceed with the incremental approach to study the instabilities of the bulk of the domain. Bear in mind that the approach detailed in this section is suitable for a generic, rectangular domain, and the problem will be particularized to the half-space, beam, and bilayer geometries in the upcoming sections. The directions of the generic rectangular domain ξ, γ, and ζ correspond to the width, height, and thickness of the domain, respectively. The domain is subjected to a uniaxial stretch λ in the ξ direction, which results in a homogeneous deformation gradient $\boldsymbol{F} = \mathrm{Diag}(\lambda, \eta, 1)$, where η is the corresponding stretch in the γ direction, and the stretch in the ζ direction remains 1 under plane-strain conditions. The two stretches, λ and η, can be related via a nonlinear Poisson ratio definition which is obtained by prescribing, for the Piola stress (equation (6)), $\boldsymbol{P} \cdot \boldsymbol{N} = \boldsymbol{0}$ on the *lateral sides*, where the unit outward normal to domain boundary $\partial\mathcal{B}_0$ is denoted by $\boldsymbol{N} = \pm\boldsymbol{e}_\gamma$, rendering the key relation:

$$\eta = \frac{\sqrt{1+\alpha}}{\sqrt{1+\alpha\lambda^2}}. \tag{8}$$

Moving forward, the finitely deformed configuration is perturbed via incremental, horizontal and vertical deformation functions δu and δv, and the stability of this perturbed configuration is studied. At the perturbed configuration, the linear momentum balance in the bulk, in the absence of body forces, presents $\mathrm{Div}\,\delta\boldsymbol{P} \doteq \boldsymbol{0}$, where the incremental Piola stress $\delta\boldsymbol{P}$ can be obtained through

$$\delta\boldsymbol{P} = \tfrac{\partial \boldsymbol{P}}{\partial \boldsymbol{F}} : \delta\boldsymbol{F} = \mu\delta\boldsymbol{F} + \mu\boldsymbol{F}^{-t}\cdot\delta\boldsymbol{F}^{t}\cdot\boldsymbol{F}^{-t} + 2\mu\alpha J^2\boldsymbol{F}^{-t} : \delta\boldsymbol{F}\boldsymbol{F}^{-t} - \mu\alpha[J^2-1]\boldsymbol{F}^{-t}\cdot\delta\boldsymbol{F}^{t}\cdot\boldsymbol{F}^{-t}. \tag{9}$$

Consequently the incremental linear momentum balance using the incremental Piola stress (9) reads:

$$\mathrm{Div}\delta\boldsymbol{P} \doteq \boldsymbol{0} \;\text{ and }\; [\delta\boldsymbol{F}] = \begin{bmatrix} \delta u_{,\xi} & \delta u_{,\gamma} \\ \delta v_{,\xi} & \delta v_{,\gamma} \end{bmatrix} \;\Rightarrow\; \begin{cases} [\delta u_{,\xi,\xi} + \delta u_{,\gamma,\gamma}] + \omega[\eta^2\delta u_{,\xi,\xi} + \lambda\eta\delta v_{,\xi,\gamma}] = 0 \\ [\delta v_{,\xi,\xi} + \delta v_{,\gamma,\gamma}] + \omega[\lambda\eta\delta u_{,\gamma,\xi} + \lambda^2\delta v_{,\gamma,\gamma}] = 0, \end{cases} \tag{10}$$

where $\omega := 1/J^2 + \alpha + \alpha/J^2$, yielding a differential equation in terms of the incremental displacement functions and their partial derivatives. The incremental displacements $\delta\boldsymbol{u} = [\delta u, \delta v]^t$ which constitute a general solution to the partial differential equation (10) read $\delta u = A\exp(r\gamma)\sin(k\xi)$ for horizontal incremental displacement, and $\delta v = B\exp(r\gamma)\cos(k\xi)$ for vertical incremental displacement, which can be expressed as

$$\delta\boldsymbol{u} = \boldsymbol{T}\boldsymbol{E}(\gamma)\Xi \text{ with } \boldsymbol{T} := \begin{bmatrix} \sin(k\xi) & 0 \\ 0 & \cos(k\xi) \end{bmatrix},\; \mathbf{E}(\gamma) := \begin{bmatrix} \exp(r\gamma) & 0 \\ 0 & \exp(r\gamma) \end{bmatrix},\; \Xi := \begin{bmatrix} A \\ B \end{bmatrix}, \tag{11}$$

where r is the *decay coefficient* for the exponential *decay function* and k is the wavenumber. Evaluating the incremental linear momentum balance (10) with the partial derivatives of the generic ansatz renders four different solutions for r, each of which can in turn be used to relate the set of constants A and B, such that $A_i = C_i(\lambda, \eta, \nu)B_i$, where C_i is a coefficient which is a function of λ, η, and ν. With only the unknown coefficients B_1, B_2, B_3, and B_4 remaining, the updated incremental displacement functions can be written succinctly as

$$\delta\boldsymbol{u} = \boldsymbol{T}^{1}_{2}\boldsymbol{G}^{1}_{2}\boldsymbol{E}(\gamma)^{1}_{2}\boldsymbol{B} + \boldsymbol{T}^{3}_{4}\boldsymbol{G}^{3}_{4}\boldsymbol{E}(\gamma)^{3}_{4}\boldsymbol{B}, \tag{12}$$

in which

$$
\begin{aligned}
{}^{1}_{2}\boldsymbol{G} &:= \begin{bmatrix} -\frac{\lambda}{\eta} & -\frac{\theta}{\lambda\eta} \\ 1 & 1 \end{bmatrix}, \quad {}^{1}_{2}\boldsymbol{E}(\gamma) := \begin{bmatrix} \exp(k\gamma) & 0 \\ 0 & \exp\left(k\sqrt{\rho}\,\gamma\right) \end{bmatrix}, \quad {}^{1}_{2}\boldsymbol{B} := \begin{bmatrix} B_1 \\ B_2 \end{bmatrix}, \\
{}^{3}_{4}\boldsymbol{G} &:= \begin{bmatrix} -\frac{\lambda}{\eta} & -\frac{\theta}{\lambda\eta} \\ 1 & 1 \end{bmatrix}, \quad {}^{3}_{4}\boldsymbol{E}(\gamma) := \begin{bmatrix} \exp(-k\gamma) & 0 \\ 0 & \exp\left(-k\sqrt{\rho}\,\gamma\right) \end{bmatrix}, \quad {}^{3}_{4}\boldsymbol{B} := \begin{bmatrix} B_3 \\ B_4 \end{bmatrix},
\end{aligned}
\tag{13}
$$

with $\rho := [1+\omega\eta^2]/[1+\omega\lambda^2]$ and $\theta := [\rho[1+\omega\lambda^2]-1]/[\omega\sqrt{\rho}]$.

With the balance equations for the bulk at hand, we now move to the interface problem, where we first need to formulate the incremental counterparts of the interface balance equations (3), which read

$$
\overline{\mathrm{Div}}\,\delta\bar{\boldsymbol{P}} + [[\delta\boldsymbol{P}]]\cdot\bar{\boldsymbol{N}} = \boldsymbol{0} \;\text{ on }\; \mathcal{I}_0\,(\text{along}) \;\text{ and }\; \delta\bar{\boldsymbol{t}} - \{\{\delta\boldsymbol{P}\}\}\cdot\bar{\boldsymbol{N}} = \boldsymbol{0} \;\text{ on }\; \mathcal{I}_0\,(\text{across}). \tag{14}
$$

In order to evaluate equation (14), we need to derive the interface counterpart of the incremental Piola stress (equation (9)), which can be obtained through

$$
\delta\bar{\boldsymbol{P}} = \frac{\partial\bar{\boldsymbol{P}}}{\partial\bar{\boldsymbol{F}}} : \delta\bar{\boldsymbol{F}} = \bar{\mu}\,[\bar{\mathbb{I}} - \bar{\mathbb{D}}] : \delta\bar{\boldsymbol{F}}, \tag{15}
$$

where

$$
\bar{\mathbb{I}} := \frac{\partial\bar{\boldsymbol{F}}}{\partial\bar{\boldsymbol{F}}} = \boldsymbol{i}\,\overline{\otimes}\,\bar{\boldsymbol{I}} \;\text{ and }\; \bar{\mathbb{D}} := \frac{\partial\bar{\boldsymbol{F}}^{-t}}{\partial\bar{\boldsymbol{F}}} = -\bar{\boldsymbol{F}}^{-t}\underline{\otimes}\bar{\boldsymbol{F}}^{-1} + [\bar{\boldsymbol{n}}\otimes\bar{\boldsymbol{n}}]\,\overline{\otimes}\,[\bar{\boldsymbol{F}}^{-1}\cdot\bar{\boldsymbol{F}}^{-t}], \tag{16}
$$

and $\bar{\boldsymbol{P}}$ is the Piola stress along the interface defined in equation (7). Accordingly, since $\bar{\mathbb{I}} : \delta\bar{\boldsymbol{F}} = \delta\bar{\boldsymbol{F}}$, the interfacial counterpart of the incremental Piola stress in equation (9) can be written as

$$
\delta\bar{\boldsymbol{P}} = \bar{\mu}\,\delta\bar{\boldsymbol{F}} + \bar{\mu}\,\bar{\boldsymbol{F}}^{-t}\cdot\delta\bar{\boldsymbol{F}}^{t}\cdot\bar{\boldsymbol{F}}^{-t} - \bar{\mu}\,\frac{1}{\lambda^2}\,\delta\bar{\boldsymbol{F}} : [\bar{\boldsymbol{n}}\otimes\boldsymbol{e}_\xi]\,\bar{\boldsymbol{n}}\otimes\boldsymbol{e}_\xi. \tag{17}
$$

Note that unit tangents to the interface *prior to the onset of instability* in both the material and spatial configurations coincide with $\boldsymbol{e}_\xi$, since before wrinkling the interface remains flat. Similarly, unit normals to the *interface* prior to the onset of instability, $\bar{\boldsymbol{N}}$ and $\bar{\boldsymbol{n}}$ in the material and spatial configurations, respectively, coincide with $\boldsymbol{e}_\gamma$ pointing upward. A similar approach can be taken to formulate the incremental interface deformation gradient $\delta\bar{\boldsymbol{F}} = \{\{\delta\boldsymbol{F}\}\}\cdot\bar{\boldsymbol{I}}$, which in matrix representation reads:

$$
[\delta\bar{\boldsymbol{F}}] = \frac{1}{2}\begin{bmatrix} \delta u_{f,\,\xi} + \delta u_{s,\,\xi} & \delta u_{f,\,\gamma} + \delta u_{s,\,\gamma} \\ \delta v_{f,\,\xi} + \delta v_{s,\,\xi} & \delta v_{f,\,\gamma} + \delta v_{s,\,\gamma} \end{bmatrix}\cdot\begin{bmatrix} 1 & 0 \\ 0 & 0 \end{bmatrix} = \frac{1}{2}\begin{bmatrix} \delta u_{f,\,\xi} + \delta u_{s,\,\xi} & 0 \\ \delta v_{f,\,\xi} + \delta v_{s,\,\xi} & 0 \end{bmatrix}. \tag{18}
$$

It should be noted that the tensor $\delta\bar{\boldsymbol{F}}$ in equation (18) has been denoted in matrix notation wherein the basis vectors correspond to the material configuration. Although a matrix notation is commonly accepted to express rank-sufficient tensors, it proves particularly problematic for rank-deficient tensors, such as $\delta\bar{\boldsymbol{F}}$ here, and therefore it results in a column of zeros associated with the derivatives with respect to the direction orthogonal to the interface. The incremental interface Piola stress (17) hence, after some mathematical simplifications, becomes

$$
[\delta\bar{\boldsymbol{P}}] = \frac{\bar{\mu}}{2\lambda^2}\begin{bmatrix} \left[\lambda^2+1\right]\delta u_{f,\,\xi} + \left[\lambda^2+1\right]\delta u_{s,\,\xi} & 0 \\ \left[\lambda^2-1\right]\delta v_{f,\,\xi} + \left[\lambda^2-1\right]\delta v_{s,\,\xi} & 0 \end{bmatrix}. \tag{19}
$$

Equipped with the interfacial incremental Piola stress relation, we can now return to the incremental interface balance equations (14) and we evaluate $\overline{\mathrm{Div}}\,\delta\bar{\boldsymbol{P}}$. The interface divergence operator indicates the divergence along the interface, which furnishes

$$
\overline{\mathrm{Div}}\,\delta\bar{\boldsymbol{P}} = \frac{\bar{\mu}}{2\lambda^2}\begin{bmatrix} \left[\lambda^2+1\right]\left[\delta u_{f,\,\xi,\,\xi} + \delta u_{s,\,\xi,\,\xi}\right] \\ \left[\lambda^2-1\right]\left[\delta v_{f,\,\xi,\,\xi} + \delta v_{s,\,\xi,\,\xi}\right] \end{bmatrix}. \tag{20}
$$

Using the updated forms of the incremental displacement functions and their partial derivatives, equation (20) can then be written explicitly as

$$\begin{aligned}\overline{\mathrm{Div}}\,\delta\bar{\boldsymbol{P}} = k_f^2\,\frac{\bar{\mu}}{2}\begin{bmatrix}\sin(k_f\xi) & 0\\ 0 & \cos(k_f\xi)\end{bmatrix}\begin{bmatrix}\left[\lambda^2+1\right]\frac{1}{\lambda\eta_f} & \left[\lambda^2+1\right]\frac{\theta_f}{\lambda^3\eta_f}\\ -\frac{\left[\lambda^2-1\right]}{\lambda^2} & -\frac{\left[\lambda^2-1\right]}{\lambda^2}\end{bmatrix}\begin{bmatrix}\exp(k_f\gamma) & 0\\ 0 & \exp\left(k_f\sqrt{\rho_f}\,\gamma\right)\end{bmatrix}\begin{bmatrix}{}^{1}B_f\\ {}^{2}B_f\end{bmatrix}\\ + k_f^2\,\frac{\bar{\mu}}{2}\begin{bmatrix}\sin(k_f\xi) & 0\\ 0 & \cos(k_f\xi)\end{bmatrix}\begin{bmatrix}-\left[\lambda^2+1\right]\frac{1}{\lambda\eta_f} & -\left[\lambda^2+1\right]\frac{\theta_f}{\lambda^3\eta_f}\\ -\frac{\left[\lambda^2-1\right]}{\lambda^2} & -\frac{\left[\lambda^2-1\right]}{\lambda^2}\end{bmatrix}\begin{bmatrix}\exp(-k_f\gamma) & 0\\ 0 & \exp\left(-k_f\sqrt{\rho_f}\,\gamma\right)\end{bmatrix}\begin{bmatrix}{}^{3}B_f\\ {}^{4}B_f\end{bmatrix}\\ + k_s^2\,\frac{\bar{\mu}}{2}\begin{bmatrix}\sin(k_s\xi) & 0\\ 0 & \cos(k_s\xi)\end{bmatrix}\begin{bmatrix}\left[\lambda^2+1\right]\frac{1}{\lambda\eta_s} & \left[\lambda^2+1\right]\frac{\theta_s}{\lambda^3\eta_s}\\ -\frac{\left[\lambda^2-1\right]}{\lambda^2} & -\frac{\left[\lambda^2-1\right]}{\lambda^2}\end{bmatrix}\begin{bmatrix}\exp(k_s\gamma) & 0\\ 0 & \exp(k_s\sqrt{\rho_s}\,\gamma)\end{bmatrix}\begin{bmatrix}{}^{1}B_s\\ {}^{2}B_s\end{bmatrix}\\ + k_s^2\,\frac{\bar{\mu}}{2}\begin{bmatrix}\sin(k_s\xi) & 0\\ 0 & \cos(k_s\xi)\end{bmatrix}\begin{bmatrix}-\left[\lambda^2+1\right]\frac{1}{\lambda\eta_s} & -\left[\lambda^2+1\right]\frac{\theta_s}{\lambda^3\eta_s}\\ -\frac{\left[\lambda^2-1\right]}{\lambda^2} & -\frac{\left[\lambda^2-1\right]}{\lambda^2}\end{bmatrix}\begin{bmatrix}\exp(-k_s\gamma) & 0\\ 0 & \exp\left(-k_s\sqrt{\rho_s}\,\gamma\right)\end{bmatrix}\begin{bmatrix}{}^{3}B_s\\ {}^{4}B_s\end{bmatrix},\end{aligned} \tag{21}$$

which can be expressed more concisely as

$$\overline{\mathrm{Div}}\,\delta\bar{\boldsymbol{P}} = \tfrac{\bar{\mu}}{2}\left[k_f^2\,\boldsymbol{T}_f\,{}^{1}_{2}\boldsymbol{M}_f\,{}^{1}_{2}\boldsymbol{E}_f(\gamma)\,{}^{1}_{2}\boldsymbol{B}_f + k_f^2\,\boldsymbol{T}_f\,{}^{3}_{4}\boldsymbol{M}_f\,{}^{3}_{4}\boldsymbol{E}_f(\gamma)\,{}^{3}_{4}\boldsymbol{B}_f + k_s^2\,\boldsymbol{T}_s\,{}^{1}_{2}\boldsymbol{M}_s\,{}^{1}_{2}\boldsymbol{E}_s(\gamma)\,{}^{1}_{2}\boldsymbol{B}_s + k_s^2\,\boldsymbol{T}_s\,{}^{3}_{4}\boldsymbol{M}_s\,{}^{3}_{4}\boldsymbol{E}_s(\gamma)\,{}^{3}_{4}\boldsymbol{B}_s\right], \tag{22}$$

where

$$\boldsymbol{T}_f = \begin{bmatrix}\sin(k_f\xi) & 0\\ 0 & \cos(k_f\xi)\end{bmatrix},\quad \boldsymbol{T}_s = \begin{bmatrix}\sin(k_s\xi) & 0\\ 0 & \cos(k_s\xi)\end{bmatrix}, \tag{23}$$

with

$$\begin{aligned}{}^{1}_{2}\boldsymbol{E}_f(\gamma) &:= \begin{bmatrix}\exp(k_f\gamma) & 0\\ 0 & \exp\left(k_f\sqrt{\rho_f}\,\gamma\right)\end{bmatrix},\quad {}^{3}_{4}\boldsymbol{E}_f(\gamma) := \begin{bmatrix}\exp(-k_f\gamma) & 0\\ 0 & \exp\left(-k_f\sqrt{\rho_f}\,\gamma\right)\end{bmatrix},\\ {}^{1}_{2}\boldsymbol{E}_s(\gamma) &:= \begin{bmatrix}\exp(k_s\gamma) & 0\\ 0 & \exp\left(k_s\sqrt{\rho_s}\,\gamma\right)\end{bmatrix},\quad {}^{3}_{4}\boldsymbol{E}_s(\gamma) := \begin{bmatrix}\exp(-k_s\gamma) & 0\\ 0 & \exp\left(-k_s\sqrt{\rho_s}\,\gamma\right)\end{bmatrix},\end{aligned} \tag{24}$$

and

$$\begin{aligned}{}^{1}_{2}\boldsymbol{M}_f &= \begin{bmatrix}\left[\lambda^2+1\right]\frac{1}{\lambda\eta_f} & \left[\lambda^2+1\right]\frac{\theta_f}{\lambda^3\eta_f}\\ -\frac{\left[\lambda^2-1\right]}{\lambda^2} & -\frac{\left[\lambda^2-1\right]}{\lambda^2}\end{bmatrix},\quad {}^{1}_{2}\boldsymbol{B}_f = \begin{bmatrix}{}^{1}B_f\\ {}^{2}B_f\end{bmatrix},\\ {}^{3}_{4}\boldsymbol{M}_f &= \begin{bmatrix}-\left[\lambda^2+1\right]\frac{1}{\lambda\eta_f} & -\left[\lambda^2+1\right]\frac{\theta_f}{\lambda^3\eta_f}\\ -\frac{\left[\lambda^2-1\right]}{\lambda^2} & -\frac{\left[\lambda^2-1\right]}{\lambda^2}\end{bmatrix},\quad {}^{3}_{4}\boldsymbol{B}_f = \begin{bmatrix}{}^{3}B_f\\ {}^{4}B_f\end{bmatrix},\end{aligned}$$

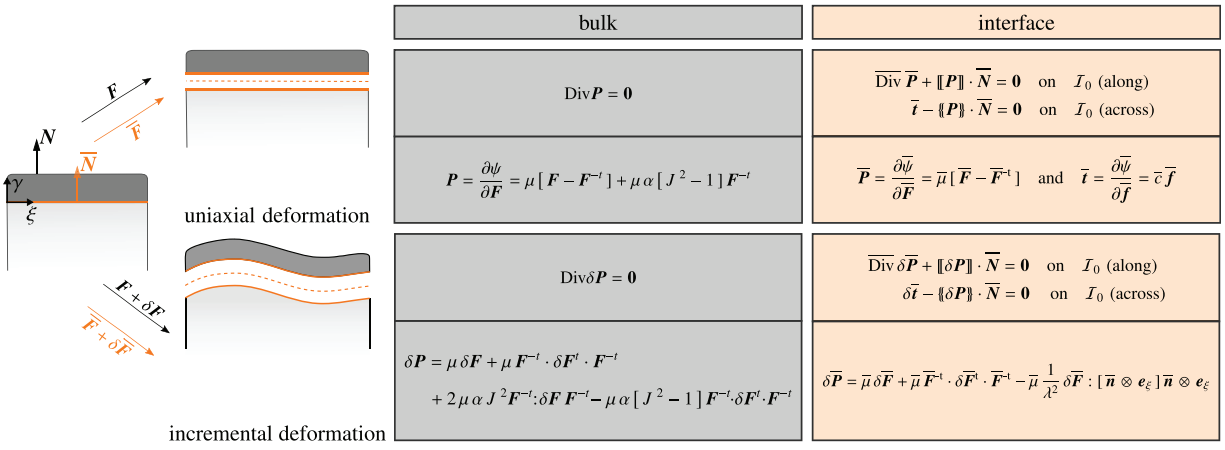

Figure 3. Table summarizing the key concepts and relations of the approach developed here.

$$
{}^{1}_{2}\boldsymbol{M}_s=\begin{bmatrix}\left[\lambda^2+1\right]\frac{1}{\lambda\eta_s} & \left[\lambda^2+1\right]\frac{\theta_s}{\lambda^3\eta_s}\\ -\frac{\left[\lambda^2-1\right]}{\lambda^2} & -\frac{\left[\lambda^2-1\right]}{\lambda^2}\end{bmatrix},\qquad {}^{1}_{2}\boldsymbol{B}_s=\begin{bmatrix}{}^{1}B_s\\ {}^{2}B_s\end{bmatrix},
$$
$$
{}^{3}_{4}\boldsymbol{M}_s=\begin{bmatrix}-\left[\lambda^2+1\right]\frac{1}{\lambda\eta_s} & -\left[\lambda^2+1\right]\frac{\theta_s}{\lambda^3\eta_s}\\ -\frac{\left[\lambda^2-1\right]}{\lambda^2} & -\frac{\left[\lambda^2-1\right]}{\lambda^2}\end{bmatrix},\qquad {}^{3}_{4}\boldsymbol{B}_s=\begin{bmatrix}{}^{3}B_s\\ {}^{4}B_s\end{bmatrix}. \tag{25}
$$

Finally, the remaining unknown coefficients B_1, B_2, B_3, and B_4 need to be solved for by imposing the displacement and traction boundary conditions of the problem at hand, since until this point, the derivations have been generic and independent of the dimensions and boundary conditions of the rectangular domain. The traction increment at an outer surface of the rectangular domain is dictated by the relation $\delta\boldsymbol{t}=\delta\boldsymbol{P}\cdot\boldsymbol{N}$; resulting in

$$
\delta\boldsymbol{t}\quad=-\mu k\,\boldsymbol{T}^{1}_{2}\boldsymbol{W}^{1}_{2}\boldsymbol{E}(\gamma)^{1}_{2}\boldsymbol{B}+\mu k\,\boldsymbol{T}^{3}_{4}\boldsymbol{W}^{3}_{4}\boldsymbol{E}(\gamma)^{3}_{4}\boldsymbol{B}, \tag{26}
$$

where

$$
-{}^{1}_{2}\boldsymbol{W}:=\begin{bmatrix}-\frac{\lambda}{\eta}-D\lambda\,\eta & -\sqrt{\rho}\,\frac{\theta}{\lambda\eta}-D\lambda\,\eta\\ -\left[1+D\lambda^2\right] & \sqrt{\rho\left[1+\omega\lambda^2\right]}-2\alpha\theta\end{bmatrix},\quad {}^{3}_{4}\boldsymbol{W}:=\begin{bmatrix}-\frac{\lambda}{\eta}-D\lambda\,\eta & -\sqrt{\rho}\,\frac{\theta}{\lambda\eta}-D\lambda\,\eta\\ -\left[1+D\lambda^2\right] & -\sqrt{\rho}\left[1+\omega\lambda^2\right]+2\alpha\theta\end{bmatrix}, \tag{27}
$$

in which $\omega:=D+2\alpha=1/J^2+\alpha+\alpha/J^2$ and $D:=1/J^2-\alpha+\alpha/J^2$. Similarly, the interface boundary conditions, according to the interface model, can be applied using the derived forms of the incremental balance equations (14).

This concludes the generic part of the incremental instability analysis, and the derived relations for the bulk and interface, together with their incremental counterparts have been summarized in Figure 3. The upcoming sections particularize the generic approach for the case of a coated half-space, coated beam, and finally a bilayer structure with a general interface model, via imposing the appropriate (boundary) conditions. Figure 4 briefly outlines and collects together these boundary conditions applied for the domains considered in this contribution, together with the boundary conditions for limit cases that can be found in literature with no interface and at the incompressible limit. This hierarchical structure elucidates the universality of the framework developed here accounting for (a) the compressibility of the domains and (b) the general interface model.

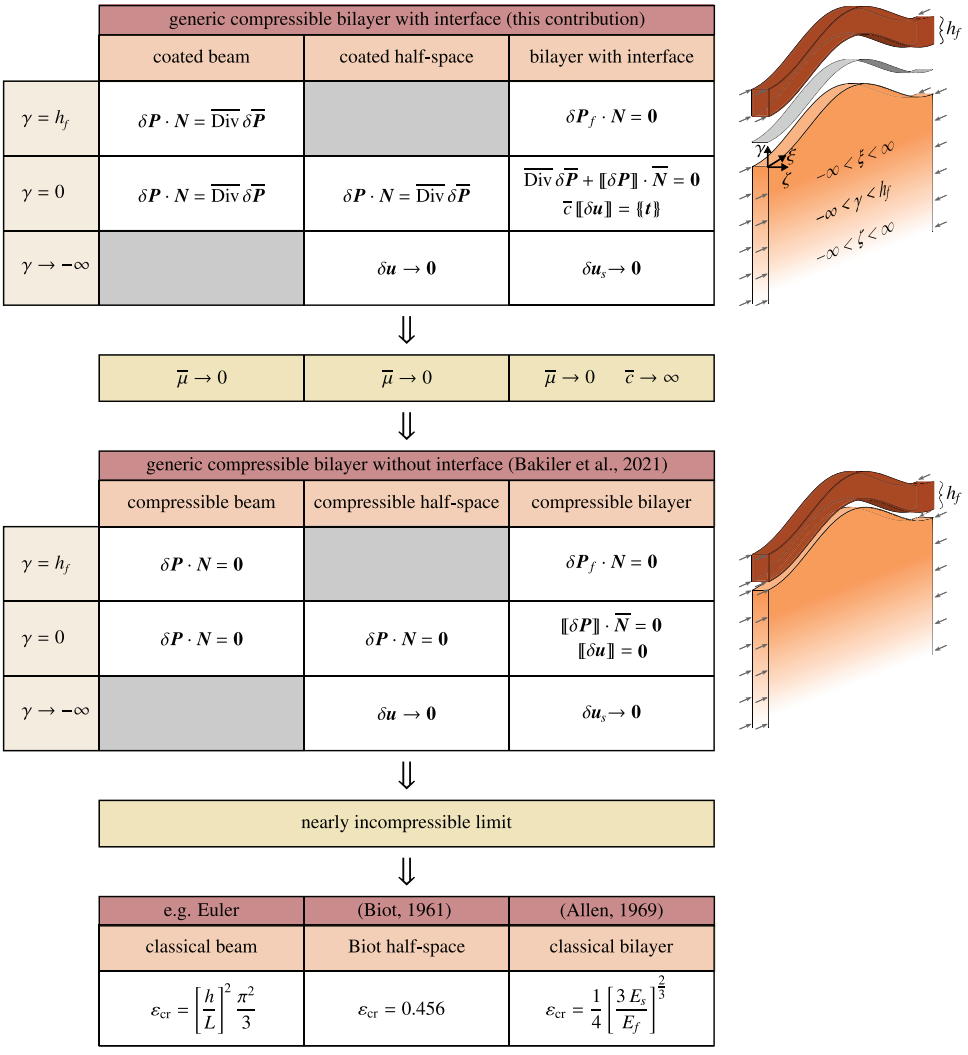

Figure 4. Summarizing the boundary conditions applied for the domains considered here, namely, for a coated beam, coated half-space, and bilayer with interface, together with the boundary conditions for limit cases of no interfacial effects and at incompressibility. This hierarchical structure elucidates the universality of the framework developed here accounting for (a) the compressibility of the domains and (b) the general interface model.

3. Coated half-space

This section particularizes the framework in Section 2 to examine the bifurcation behavior of a coated half-space. We start off by imposing that the domain is a half-space, which dictates that the incremental displacements $\delta \boldsymbol{u}$ should decay as the domain depth $\gamma \to -\infty$. Imposing this condition yields the set of constants ${}^{3}_{4}\boldsymbol{B}$ to be zero, resulting in the incremental displacement profile of

$$\delta \boldsymbol{u} \quad = \boldsymbol{T}^{1}_{2} \boldsymbol{G}^{1}_{2} \boldsymbol{E}(\gamma)^{1}_{2} \boldsymbol{B}. \tag{28}$$

The boundary on the top surface of the half-space is coated with an elastic interface or rather surface, resulting in

$$\delta \boldsymbol{P} \cdot \overline{\boldsymbol{N}}|_{\gamma = 0} = \overline{\mathrm{Div}}\, \delta \overline{\boldsymbol{P}}, \tag{29}$$

where $\overline{\mathrm{Div}}\,\delta\overline{\boldsymbol{P}}$ for the half-space reads

$$\begin{aligned}\overline{\mathrm{Div}}\,\delta\overline{\boldsymbol{P}} &= \frac{\overline{\mu}}{\lambda^2}\begin{bmatrix}\left[\lambda^2+1\right]\delta u_{,\,\xi,\,\xi}\\ \left[\lambda^2-1\right]\delta v_{,\,\xi,\,\xi}\end{bmatrix}\\ &= k^2\overline{\mu}\begin{bmatrix}\sin(k\xi) & 0\\ 0 & \cos(k\xi)\end{bmatrix}\begin{bmatrix}\left[\lambda^2+1\right]\frac{1}{\lambda\eta} & \left[\lambda^2+1\right]\frac{\theta}{\lambda^3\eta}\\ -\frac{\left[\lambda^2-1\right]}{\lambda^2} & -\frac{\left[\lambda^2-1\right]}{\lambda^2}\end{bmatrix}\begin{bmatrix}\exp(k\gamma) & 0\\ 0 & \exp\left(k\sqrt{\rho}\,\gamma\right)\end{bmatrix}\begin{bmatrix}{}^{1}B\\ {}^{2}B\end{bmatrix},\end{aligned} \tag{30}$$

or in its shorter form:

$$\overline{\mathrm{Div}}\,\delta\bar{\boldsymbol{P}} \quad = k^2\,\bar{\mu}\,\boldsymbol{T}^{\frac{1}{2}}\boldsymbol{M}^{\frac{1}{2}}\boldsymbol{E}(\gamma)^{\frac{1}{2}}\boldsymbol{B}, \tag{31}$$

rendering the balance equation at $\gamma = 0$ to be

$$-\mu k\,\boldsymbol{T}^{\frac{1}{2}}\boldsymbol{W}^{\frac{1}{2}}\boldsymbol{B} = k^2\,\bar{\mu}\,\boldsymbol{T}^{\frac{1}{2}}\boldsymbol{M}^{\frac{1}{2}}\boldsymbol{B}. \tag{32}$$

Simplifying and rearranging equation (32) yield the final solution

$$\boldsymbol{Q}^{\frac{1}{2}}\boldsymbol{B} = \boldsymbol{0} \;\text{ where }\; \boldsymbol{Q} := \left[f\,{}^{\frac{1}{2}}\boldsymbol{M} + {}^{\frac{1}{2}}\boldsymbol{W}\right] \;\text{ with }\; f := k\,\frac{\bar{\mu}}{\mu}, \tag{33}$$

in which f has been defined as a dimensionless parameter for the sake of convenience. The system (33) can be solved via setting $\mathrm{Det}\,\boldsymbol{Q}(k,\lambda) \doteq 0$ and thus solving for the critical stretch λ_{cr}. This system is solved for a range of values of k, and the value of k which renders the highest λ_{cr}, hence the initial instability mode encountered when compressing a domain starting from the reference configuration $\lambda = 1$, and its corresponding wavenumber k_{cr} is sought for. In other words, $\lambda_{cr} = \max\{\lambda \,|\, \mathrm{Det}\,\boldsymbol{Q}(k,\lambda) = 0, \forall k \in \mathbb{R}^+\}$.

At this point, it proves useful to look at certain limits of the obtained solution. For instance, $\bar{\mu} = 0$ renders the coating-free half-space solution; in other words,

$$\bar{\mu} = 0 \;\Rightarrow\; f = 0 \;\Rightarrow\; {}^{\frac{1}{2}}\boldsymbol{W}^{\frac{1}{2}}\boldsymbol{B} = \boldsymbol{0} \;\Rightarrow\; \mathrm{Det}\,{}^{\frac{1}{2}}\boldsymbol{W} \doteq 0, \tag{34}$$

which coincides with the findings in Bakiler et al. [29]. For the case that $\bar{\mu} \neq 0$, so in the presence of coating, there are two limits to be explored, namely, (a) $k = 0$ and (b) $k \to \infty$. It can be seen clearly that at $k = 0$, the defined parameter $f = 0$ once again, and the half-space solution is obtained. For the case of $k \to \infty$, we can see that equation (32) reduces to

$$k \to \infty \;\Rightarrow\; {}^{\frac{1}{2}}\boldsymbol{M}^{\frac{1}{2}}\boldsymbol{B} = \boldsymbol{0} \;\Rightarrow\; \mathrm{Det}\,{}^{\frac{1}{2}}\boldsymbol{M} \doteq 0 \;\Rightarrow\; -\frac{\left[\lambda^2+1\right]\left[\lambda^2-1\right]}{\lambda^3\eta} + \frac{\theta\left[\lambda^2+1\right]\left[\lambda^2-1\right]}{\lambda^5\eta} \doteq 0, \tag{35}$$

or alternatively expressed as

$$-\left[\lambda^2+1\right]\left[\lambda^2-1\right]\left[\theta-\lambda^2\right] \doteq 0, \tag{36}$$

which clearly has one trivial root at $\lambda = 1$. To see if the expression (36) has another root, we insert the expression for θ and study its consequences. That is,

$$\theta - \lambda^2 = \frac{\rho\left[1+\omega\lambda^2\right]-1}{\omega\sqrt{\rho}} - \lambda^2 = \frac{\frac{\left[1+\omega\eta^2\right]}{\left[1+\omega\lambda^2\right]}\left[1+\omega\lambda^2\right]-1}{\omega\sqrt{\rho}} - \lambda^2 = \frac{\eta^2-\lambda^2\sqrt{\rho}}{\sqrt{\rho}} \;\Rightarrow\; \eta^2 - \lambda^2\sqrt{\rho} \doteq 0. \tag{37}$$

The term $\sqrt{\rho}$ can be simplified to

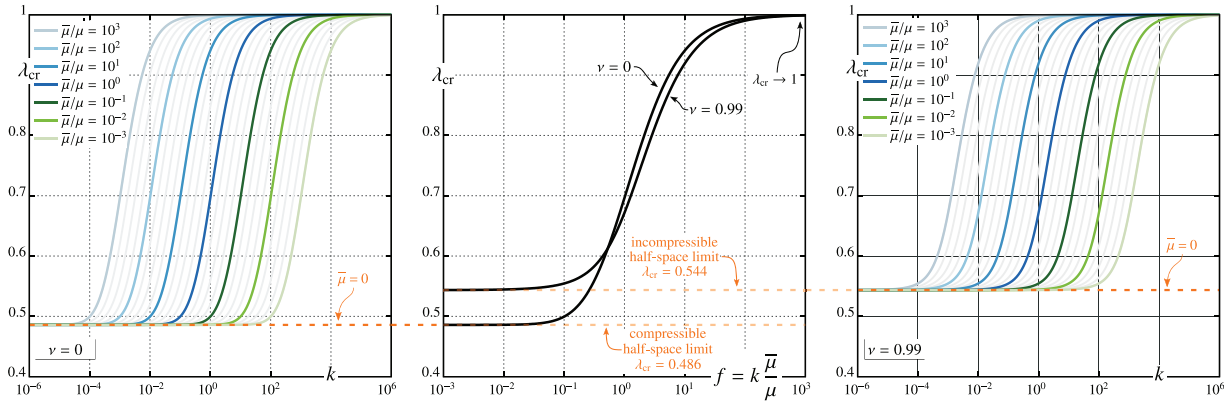

Figure 5. Bifurcation curves for a coated half-space, that is, the solutions for the system $\mathrm{Det}\,\mathbf{Q}(k,\lambda) \doteq 0$ for λ_{cr} over changing wavenumber k for fully compressible (left) and nearly incompressible (right) half-space, and plotted against dimensionless parameter $f = k\bar{\mu}/\mu$ (center) for both $\nu = 0$ and $\nu = 0.99$. Again, note that the plane-strain definition of Poisson's ratio is employed. That is, excluding the auxetic regime, $0 \leqslant \nu < 1$, where $\nu = 0$ indicates full compressibility and $\nu \to 1$ indicates incompressibility. This plane-strain definition relates to its 3D counterpart such that $\nu_{3D} = \nu/(1+\nu)$.

$$\sqrt{\rho} = \frac{\eta}{\lambda}\sqrt{\frac{\lambda^2 + 1 + \alpha\lambda^2 + \alpha}{\eta^2 + 1 + \alpha\eta^2 + \alpha}}, \tag{38}$$

which renders equation (37) to be

$$\eta - \lambda\sqrt{\frac{\lambda^2 + 1 + \alpha\lambda^2 + \alpha}{\eta^2 + 1 + \alpha\eta^2 + \alpha}} \doteq 0 \;\Rightarrow\; \eta - \lambda\sqrt{\frac{\lambda^2 + 1}{\eta^2 + 1}} \doteq 0 \;\Rightarrow \eta^2\left[\eta^2 + 1\right] = \lambda^2\left[\lambda^2 + 1\right]. \tag{39}$$

For the problem at hand, (a) $0 < \lambda \leqslant 1$, since we apply compression, (b) $0 \leqslant \alpha < \infty$, for nonauxetic materials, which together, via equation (8), mean that (c) $\eta \geqslant 1$. Given all of these, one can see that the expression (39) and more importantly equation (36) is *only* satisfied when $\lambda = \eta = 1$. Hence, we have shown that for any $\bar{\mu} \neq 0$, there exists always, and only, the solution $\lambda_{cr} = 1$ at $k \to \infty$, apart from the trivial solution. This outcome matches the findings of Steigmann and Ogden [26], and in other words means that unless surface elasticity is vanishing, a coated half-space, or rather the interface on top, will buckle with infinite wavenumber right at the start of compression. The limits of $k \to 0$ and $k \to \infty$ can also be seen in Figure 5, where λ_{cr} has been plotted with respect to wavenumber k and the dimensionless parameter f for a fully compressible (left) and nearly incompressible (right) half-space. When plotted against f, the bifurcation curves for all parameters $\bar{\mu}/\mu$ converge to a single curve. The bifurcation curves shown in Figure 5 portray clearly that unless $\bar{\mu} = 0$, the first bifurcation mode encountered would be at $\lambda_{cr} = 1$ and $k_{cr} \to \infty$.

4. Coated beam

This section particularizes the framework developed in Section 2 to investigate the buckling of a coated beam, of length L and thickness h. First off, we need to define some of the interface quantities for the case of a coated beam, such as the incremental deformation gradient along the interface $\delta\bar{\boldsymbol{F}}$, which can be obtained via $\delta\bar{\boldsymbol{F}} = \{\{\delta\boldsymbol{F}\}\} \cdot \bar{\boldsymbol{I}}$ which for the case of a coated beam reads simply $\delta\bar{\boldsymbol{F}} = \delta\boldsymbol{F} \cdot \bar{\boldsymbol{I}}$, where

$$\delta\bar{\boldsymbol{F}} = \begin{bmatrix} \delta u_{,\xi} & 0 \\ \delta v_{,\xi} & 0 \end{bmatrix}. \tag{40}$$

Using the derived form of the interfacial incremental stress and particularizing it to the case of a coated beam,

$$\overline{\mathrm{Div}}\,\delta\bar{\boldsymbol{P}} \quad = \frac{\bar{\mu}}{\lambda^2}\begin{bmatrix}\left[\lambda^2+1\right]\delta u_{,\,\xi,\,\xi}\\ \left[\lambda^2-1\right]\delta v_{,\,\xi,\,\xi}\end{bmatrix}, \tag{41}$$

which can be written as

$$\overline{\mathrm{Div}}\,\delta\bar{\boldsymbol{P}} = k^2\,\bar{\mu}\left[\boldsymbol{T}^{1}_{2}\boldsymbol{M}^{1}_{2}\boldsymbol{E}(\gamma)^{1}_{2}\boldsymbol{B} + \boldsymbol{T}^{3}_{4}\boldsymbol{M}^{3}_{4}\boldsymbol{E}(\gamma)^{3}_{4}\boldsymbol{B}\right]. \tag{42}$$

The boundary condition on the upper surface of the beam reads:

$$\delta\boldsymbol{P}\cdot\boldsymbol{N}|_{\gamma=h} = \overline{\mathrm{Div}}\,\delta\bar{\boldsymbol{P}}, \tag{43}$$

where the unit normal to the surface is $\boldsymbol{N}=\boldsymbol{e}_{\gamma}$. Using the expression for incremental Piola stress in equation (43) results in

$$-\mu k\,\boldsymbol{T}^{1}_{2}\boldsymbol{W}^{1}_{2}\boldsymbol{E}\big(h_f\big)^{1}_{2}\boldsymbol{B} + \mu k\,\boldsymbol{T}^{3}_{4}\boldsymbol{W}^{3}_{4}\boldsymbol{E}\big(h_f\big)^{3}_{4}\boldsymbol{B} = k^2\,\bar{\mu}\,\boldsymbol{T}^{1}_{2}\boldsymbol{M}^{1}_{2}\boldsymbol{E}\big(h_f\big)^{1}_{2}\boldsymbol{B} + k^2\bar{\mu}\,\boldsymbol{T}^{3}_{4}\boldsymbol{M}^{3}_{4}\boldsymbol{E}\big(h_f\big)^{3}_{4}\boldsymbol{B}, \tag{44}$$

which when simplified yields

$$-^{1}_{2}\boldsymbol{W}^{1}_{2}\boldsymbol{E}\big(h_f\big)^{1}_{2}\boldsymbol{B} + ^{3}_{4}\boldsymbol{W}^{3}_{4}\boldsymbol{E}\big(h_f\big)^{3}_{4}\boldsymbol{B} = f^{1}_{2}\boldsymbol{M}^{1}_{2}\boldsymbol{E}\big(h_f\big)^{1}_{2}\boldsymbol{B} + f^{3}_{4}\boldsymbol{M}^{3}_{4}\boldsymbol{E}\big(h_f\big)^{3}_{4}\boldsymbol{B}. \tag{45}$$

Moving to the bottom of the beam, the traction boundary condition at $\gamma=0$ can be written as

$$\delta\boldsymbol{P}\cdot\boldsymbol{N}|_{\gamma=0} = \overline{\mathrm{Div}}\,\delta\bar{\boldsymbol{P}}, \tag{46}$$

where the unit normal to the surface now reads $\boldsymbol{N}=-\boldsymbol{e}_{\gamma}$, leading to

$$\mu k\,\boldsymbol{T}^{1}_{2}\boldsymbol{W}^{1}_{2}\boldsymbol{B} - \mu k\,\boldsymbol{T}^{3}_{4}\boldsymbol{W}^{3}_{4}\boldsymbol{B} = k^2\,\bar{\mu}\,\boldsymbol{T}^{1}_{2}\boldsymbol{M}^{1}_{2}\boldsymbol{B} + k^2\,\bar{\mu}\,\boldsymbol{T}^{3}_{4}\boldsymbol{M}^{3}_{4}\boldsymbol{B}, \tag{47}$$

which can be simplified as

$$^{1}_{2}\boldsymbol{W}^{1}_{2}\boldsymbol{B} - ^{3}_{4}\boldsymbol{W}^{3}_{4}\boldsymbol{B} = f^{1}_{2}\boldsymbol{M}^{1}_{2}\boldsymbol{B} + f^{3}_{4}\boldsymbol{M}^{3}_{4}\boldsymbol{B}, \tag{48}$$

rendering the relation

$$^{3}_{4}\boldsymbol{B} = \boldsymbol{b}^{1}_{2}\boldsymbol{B} \;\text{ with }\; \boldsymbol{b} := \left[^{3}_{4}\boldsymbol{W} + f^{3}_{4}\boldsymbol{M}\right]^{-1}\left[^{1}_{2}\boldsymbol{W} - f^{1}_{2}\boldsymbol{M}\right]. \tag{49}$$

Once again, $f := k\bar{\mu}/\mu$ is defined as previously. Finally, using the obtained relation (49) in the traction condition (45) results in

$$\left[^{1}_{2}\boldsymbol{W}^{1}_{2}\boldsymbol{E}\big(h_f\big) - ^{3}_{4}\boldsymbol{W}^{3}_{4}\boldsymbol{E}\big(h_f\big)\boldsymbol{b} + f\left[^{1}_{2}\boldsymbol{M}^{1}_{2}\boldsymbol{E}\big(h_f\big) + ^{3}_{4}\boldsymbol{M}^{3}_{4}\mathbf{E}\big(h_f\big)\boldsymbol{b}\right]\right]^{1}_{2}\boldsymbol{B} = \boldsymbol{0}, \tag{50}$$

which can be expressed as $\boldsymbol{Q}^{1}_{2}\boldsymbol{B}_f = \boldsymbol{0}$, too. The beam considered here is under a clamped–clamped boundary condition. Imposing this final boundary condition on the incremental displacement functions renders

$$\begin{cases}\delta u|_{\xi=0} = \delta u|_{\xi=L} = 0 & \Rightarrow \quad \sin(kL) = 0 \quad \Rightarrow \quad k = \frac{n\pi}{L},\\ \delta v|_{\xi=0} = \delta v|_{\xi=L} & \Rightarrow \quad \cos(k0) = \cos(kL) \quad \Rightarrow \quad k = \frac{2n\pi}{L},\end{cases} \tag{51}$$

resulting in the wavenumber $k = 2n\pi/L$. Solving for the nontrivial solutions of equation (50) via setting the determinant of the coefficient matrix of $^{1}_{2}\boldsymbol{B}$ to zero, for λ at various values of n, and finding the wavenumber which would render the maximum stretch give us the critical stretch λ_{cr} and the corresponding critical wavenumber k_{cr} at which bifurcation takes place.

Similar to the approach adopted in Section 3, looking at the limits of the developed solution proves useful. If there is no surface elasticity, that is, if $f=0$, then the solution converges to the beam solution that has been established previously in Bakiler et al. [29]. That is,

$$\bar{\mu}=0 \;\;\Rightarrow\;\; f=0 \;\;\Rightarrow\;\; \left[{}^{1}_{2}\boldsymbol{W}\,{}^{1}_{2}\boldsymbol{E}\left(h_f\right)-{}^{3}_{4}\boldsymbol{W}\,{}^{3}_{4}\boldsymbol{E}\left(h_f\right)\boldsymbol{b}\right]{}^{1}_{2}\boldsymbol{B}=\boldsymbol{0}. \tag{52}$$

Since the solution is maximized with respect to wavenumber k, next we look at the behavior of the solution as $k\to\infty$, which renders $f\to\infty$ for all $\bar{\mu}/\mu$, yielding

$$k\to\infty \;\;\Rightarrow\;\; \tfrac{1}{f}\to 0 \;\;\Rightarrow\;\; \left[{}^{1}_{2}\boldsymbol{M}\,{}^{1}_{2}\boldsymbol{E}\left(h_f\right)+{}^{3}_{4}\boldsymbol{M}\,{}^{3}_{4}\boldsymbol{E}\left(h_f\right)\boldsymbol{b}\right]{}^{1}_{2}\boldsymbol{B}=\boldsymbol{0}. \tag{53}$$

It can be shown that the quantity defined as $\boldsymbol{b}$ is finite as $f\to\infty$. Furthermore, given the coefficients of decay in ${}^{1}_{2}\boldsymbol{E}(h_f)$ and ${}^{3}_{4}\boldsymbol{E}(h_f)$, positive and negative, respectively, as $f\to\infty$, the former increases without bounds and the latter approaches $\boldsymbol{0}$. Thus, the expression (53) simplifies to

$${}^{1}_{2}\boldsymbol{M}\,{}^{1}_{2}\boldsymbol{E}\left(h_f\right){}^{1}_{2}\boldsymbol{B}=\boldsymbol{0}, \tag{54}$$

the roots of which can clearly be obtained by solving for $\mathrm{Det}\,{}^{1}_{2}\boldsymbol{M}=0$, rendering the exact same condition as equation (36). Following through with the same steps in Section 4, one can show that if $k\to\infty$, the expression (54) has only the root at $\lambda_{cr}=1$. Thus, in the presence of only surface elasticity, a coated beam under compression will buckle with infinite wavenumber, right at the start of compression, that is, at $\lambda_{cr}=1$.

5. Bilayer domain with interface

In this section, the interface between the film and the substrate in a bilayer structure corresponds to the general interface model, accounting for both nonzero displacement and traction jumps. Equipped with the generic tools required for the evaluation of the stability behavior of a rectangular, compressible domain, we can now apply the necessary boundary conditions and look at the interface mechanics associated with a bilayer structure. At the interface between two layers, there are two conditions which need to be addressed; namely, that of (a) displacement jump and (b) traction jump. Using the relations and their interface counterparts given in Section 2, we can now apply the boundary conditions for a bilayer structure consisting of a film and a half-space. The top surface of the bilayer structure, at $\gamma=h_f$ where h_f is film thickness, is traction free, rendering

$$\delta\boldsymbol{P}_f\cdot\boldsymbol{N}\big|_{\gamma=h_f}\doteq\boldsymbol{0}, \tag{55}$$

in which using the derived expression for traction (26) results in

$$-\mu_f k_f\,\boldsymbol{T}_f\,{}^{1}_{2}\boldsymbol{W}_f\,{}^{1}_{2}\boldsymbol{E}_f\left(h_f\right){}^{1}_{2}\boldsymbol{B}_f+\mu_f k_f\,\boldsymbol{T}_f\,{}^{3}_{4}\boldsymbol{W}_f\,{}^{3}_{4}\boldsymbol{E}_f\left(h_f\right){}^{3}_{4}\boldsymbol{B}_f=\boldsymbol{0}, \tag{56}$$

yielding the relation

$${}^{3}_{4}\boldsymbol{B}_f=\boldsymbol{b}\,{}^{1}_{2}\boldsymbol{B}_f \;\;\text{where}\;\; \boldsymbol{b}:=\left[{}^{3}_{4}\boldsymbol{W}_f\,{}^{3}_{4}\boldsymbol{E}_f(h_f)\right]^{-1}{}^{1}_{2}\boldsymbol{W}_f\,{}^{1}_{2}\boldsymbol{E}_f\left(h_f\right), \tag{57}$$

relating the unknown sets of constants ${}^{1}_{2}\boldsymbol{B}_f$ and ${}^{3}_{4}\boldsymbol{B}_f$. Furthermore, since the substrate is considered here to be a half-space, the incremental displacements should decay through the substrate depth; in other words,

$$\delta\boldsymbol{u}_s=\boldsymbol{0} \;\;\text{as}\;\; \gamma\to-\infty. \tag{58}$$

Imposing this boundary condition results in the constants ${}^{3}_{4}\boldsymbol{B}_s$ to vanish identically, given the sign of the decay coefficients in their associated decay functions.

Moving onto the interface between the film and the substrate, the traction and displacement boundary conditions need to be imposed, using the general interface model. Accordingly, at the interface, the traction jump can be written as

$$\begin{aligned}[[\delta \boldsymbol{P}]] \cdot \bar{\boldsymbol{N}}|_{\gamma=0} &= \left[\delta \boldsymbol{P}_f - \delta \boldsymbol{P}_s\right] \cdot \bar{\boldsymbol{N}}, \\ &= \mu_f k_f \boldsymbol{T}_f \left[-{}^{1}_{2}\boldsymbol{W}_f + {}^{3}_{4}\boldsymbol{W}_f \boldsymbol{b}\right] {}^{1}_{2}\boldsymbol{B}_f + \mu_s k_s \boldsymbol{T}_s {}^{1}_{2}\boldsymbol{W}_s {}^{1}_{2}\boldsymbol{B}_s,\end{aligned} \tag{59}$$

where the relation obtained in equation (57) has been used. Following the incremental form of the balance equation along the interface (14) and thus using the traction jump at the interface (59) and the form for $\overline{\mathrm{Div}}\,\delta\overline{\boldsymbol{P}}$ that has been obtained in equation (22), together with the results of the boundary conditions (57) and (58), we obtain

$$\tfrac{\bar{\mu}}{2} k_f^2 \boldsymbol{T}_f \left[{}^{1}_{2}\boldsymbol{M}_f + {}^{3}_{4}\boldsymbol{M}_f \boldsymbol{b}\right] {}^{1}_{2}\boldsymbol{B}_f + \tfrac{\bar{\mu}}{2} k_s^2 \boldsymbol{T}_s {}^{1}_{2}\boldsymbol{M}_s {}^{1}_{2}\boldsymbol{B}_s + \mu_f k_f \boldsymbol{T}_f \left[-{}^{1}_{2}\boldsymbol{W}_f + {}^{3}_{4}\boldsymbol{W}_f \boldsymbol{b}\right] {}^{1}_{2}\boldsymbol{B}_f + \mu_s k_s \boldsymbol{T}_s {}^{1}_{2}\boldsymbol{W}_s {}^{1}_{2}\boldsymbol{B}_s = \boldsymbol{0}, \tag{60}$$

which after some simplification and rearranging yields

$$\tfrac{k_f}{k_s} \boldsymbol{T}_s^{-1} \boldsymbol{T}_f \left[k_f \tfrac{\bar{\mu}}{\mu_s} \tfrac{1}{2} \left[{}^{1}_{2}\boldsymbol{M}_f + {}^{3}_{4}\boldsymbol{M}_f \boldsymbol{b}\right] - \tfrac{\mu_f}{\mu_s} \left[{}^{1}_{2}\boldsymbol{W}_f - {}^{3}_{4}\boldsymbol{W}_f \boldsymbol{b}\right]\right] {}^{1}_{2}\boldsymbol{B}_f + \left[{}^{1}_{2}\boldsymbol{W}_s + k_s \tfrac{\bar{\mu}}{\mu_s} \tfrac{1}{2} {}^{1}_{2}\boldsymbol{M}_s\right] {}^{1}_{2}\boldsymbol{B}_s = \boldsymbol{0}. \tag{61}$$

For the displacement boundary condition, we need to impose a condition which relates the displacement jump to the traction at the interface, commonly referred to as traction-separation law. That is,

$$\bar{c}\,[[\delta \boldsymbol{u}]] = \{\{\boldsymbol{t}\}\}, \tag{62}$$

which renders

$$\bar{c}\left[\boldsymbol{T}_f {}^{1}_{2}\boldsymbol{G}_f {}^{1}_{2}\boldsymbol{B}_f + \boldsymbol{T}_f {}^{3}_{4}\boldsymbol{G}_f {}^{3}_{4}\boldsymbol{B}_f - \boldsymbol{T}_s {}^{1}_{2}\boldsymbol{G}_s {}^{1}_{2}\boldsymbol{B}_s\right] = \frac{1}{2}\left[-\mu_s k_s \boldsymbol{T}_s {}^{1}_{2}\boldsymbol{W}_s {}^{1}_{2}\boldsymbol{B}_s - \mu_f k_f \boldsymbol{T}_f {}^{1}_{2}\boldsymbol{W}_f {}^{1}_{2}\boldsymbol{B}_f + \mu_f k_f \boldsymbol{T}_f {}^{3}_{4}\boldsymbol{W}_f {}^{3}_{4}\boldsymbol{B}_f\right], \tag{63}$$

and can be rearranged into

$$-\boldsymbol{T}_s \left[{}^{1}_{2}\boldsymbol{G}_s - \tfrac{\mu_s}{2\bar{c}} k_s {}^{1}_{2}\boldsymbol{W}_s\right] {}^{1}_{2}\boldsymbol{B}_s = -\boldsymbol{T}_f \left[\tfrac{\mu_f}{2\bar{c}} k_f {}^{1}_{2}\boldsymbol{W}_f - \tfrac{\mu_f}{2\bar{c}} k_f {}^{3}_{4}\boldsymbol{W}_f \boldsymbol{b} + {}^{1}_{2}\boldsymbol{G}_f + {}^{3}_{4}\boldsymbol{G}_f \boldsymbol{b}\right] {}^{1}_{2}\boldsymbol{B}_f, \tag{64}$$

yielding the relation

$${}^{1}_{2}\boldsymbol{B}_s = \boldsymbol{A}_s^{-1} \boldsymbol{T}_s^{-1} \boldsymbol{T}_f \boldsymbol{A}_f {}^{1}_{2}\boldsymbol{B}_f, \tag{65}$$

where

$$\boldsymbol{A}_f := \left[{}^{1}_{2}\boldsymbol{G}_s - \frac{\mu_s}{2\bar{c}} k_s {}^{1}_{2}\boldsymbol{W}_s\right], \quad \boldsymbol{A}_s := \left[\frac{\mu_f}{2\bar{c}} k_f {}^{1}_{2}\boldsymbol{W}_f - \frac{\mu_f}{2\bar{c}} k_f {}^{3}_{4}\boldsymbol{W}_f \boldsymbol{b} + {}^{1}_{2}\boldsymbol{G}_f + {}^{3}_{4}\boldsymbol{G}_f \boldsymbol{b}\right]. \tag{66}$$

Finally, using the relation (65) in the traction condition (61), we can obtain

$$\begin{aligned}&\frac{k_f}{k_s} \boldsymbol{T}_s^{-1} \boldsymbol{T}_f \left[k_f \frac{\bar{\mu}}{\mu_s} \frac{1}{2} \left[{}^{1}_{2}\boldsymbol{M}_f + {}^{3}_{4}\boldsymbol{M}_f \boldsymbol{b}\right] - \frac{\mu_f}{\mu_s} \left[{}^{1}_{2}\boldsymbol{W}_f - {}^{3}_{4}\boldsymbol{W}_f \boldsymbol{b}\right]\right] {}^{1}_{2}\boldsymbol{B}_f \\ &\quad + \left[{}^{1}_{2}\boldsymbol{W}_s + k_s \frac{\bar{\mu}}{\mu_s} \frac{1}{2} {}^{1}_{2}\boldsymbol{M}_s\right] \boldsymbol{A}_s^{-1} \boldsymbol{T}_s^{-1} \boldsymbol{T}_f \boldsymbol{A}_f {}^{1}_{2}\boldsymbol{B}_f = \boldsymbol{0}.\end{aligned} \tag{67}$$

Looking at the obtained form (67), we can see that the system remains dependent on the coordinate ξ, and hence virtually unsolvable, since the matrices $\boldsymbol{T}_f$ and $\boldsymbol{T}_s$ still remain in the equation in the form $\boldsymbol{T}_s^{-1}\boldsymbol{T}_f$. Thus, the relation that $k = k_f = k_s$ is imposed herein, rendering $\boldsymbol{T}_s^{-1}\boldsymbol{T}_f = \boldsymbol{I}$, implying that the

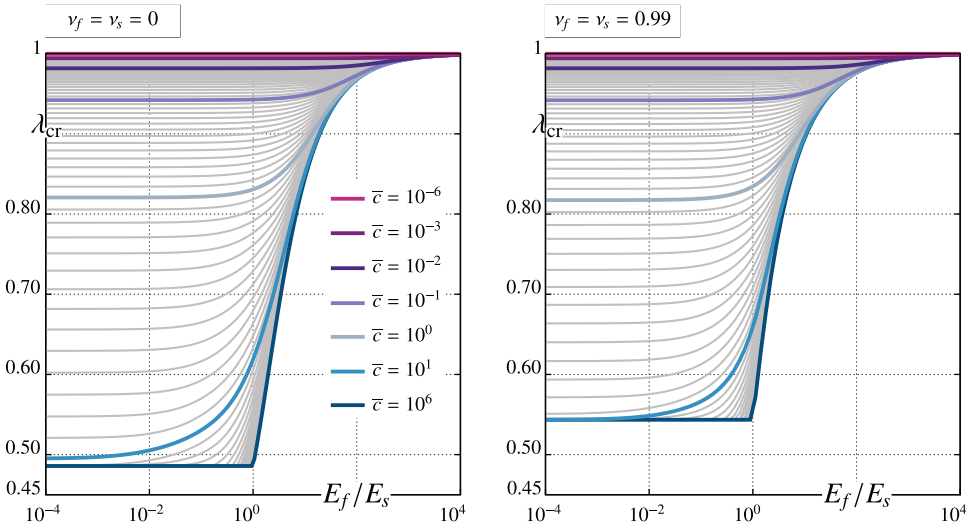

Figure 6. Critical stretch λ_{cr} versus film-to-substrate stiffness ratio E_f/E_s, plotted over a range of cohesive stiffness $\bar{c}$, for a fully compressible bilayer structure with $h_f = 1$ and $\nu_f = \nu_s = 0$ (left), and an incompressible one with $\nu_f = \nu_s = 0.99$ (right). As $\bar{c} \to \infty$, the classical bilayer case is recovered.

wavenumber of the two layers is identical. This imposition is later verified via numerical results, as well. Finally, we can obtain the familiar relation:

$$\boldsymbol{Q}^{\frac{1}{2}}\boldsymbol{B}_f = \boldsymbol{0}, \tag{68}$$

where

$$\boldsymbol{Q} := \left[{}^{\frac{1}{2}}\boldsymbol{W}_s\,\boldsymbol{A}_s{}^{-1}\,\boldsymbol{A}_f - \tfrac{\mu_f}{\mu_s}\,{}^{\frac{1}{2}}\boldsymbol{W}_f + \tfrac{\mu_f}{\mu_s}\,{}^{\frac{3}{4}}\boldsymbol{W}_f\,\boldsymbol{b} + \tfrac{\bar{\mu}}{2\mu_s}\left[k_s\,{}^{\frac{1}{2}}\boldsymbol{M}_s\,\boldsymbol{A}_s{}^{-1}\,\boldsymbol{A}_f + k_f\,{}^{\frac{1}{2}}\boldsymbol{M}_f + k_f\,{}^{\frac{3}{4}}\boldsymbol{M}_f\,\boldsymbol{b}\right]\right]. \tag{69}$$

The system (68) can be solved by setting the determinant of $\boldsymbol{Q}$ to zero and solving for the critical stretch λ_{cr} which satisfies this equality. However, the system still remains a function of the wavenumber k, and of the vertical stretches η_f and η_s. Hence, the nonlinear Poisson relation (8) which relates the vertical stretch η to compressibility parameter α and horizontal stretch λ is used herein to render equation (68) only a function of λ and k. This system is then solved for a range of values of k, and the value of k which renders the highest λ_{cr}, that is, the first mode of instability and its corresponding wavenumber k_{cr} that is encountered when compressing a domain from $\lambda = 1$, is sought for, that is, $\lambda_{cr} = \max\{\lambda \,|\, \mathrm{Det}\,\boldsymbol{Q}(k,\lambda) = 0, \forall k \in \mathbb{R}^+\}$. From previous observations also, we realize that no matter what the cohesive stiffness $\bar{c}$ is, as long as $\bar{\mu} \neq 0$, the structure will buckle immediately at $\lambda_{cr} = 1$, with infinite wavelength. This follows from the fact that the elastic interface implemented here does not have flexural resistance due to its zero-thickness structure; thus, it fundamentally cannot provide any resistance toward compression and hence buckles immediately. One can introduce a flexural resistance to the interface model following the pioneering contribution of Steigmann and Ogden [73]; however, such an extension is out of the scope of the current study. We therefore explore the effect of cohesive stiffness $\bar{c}$ on the bifurcation of a compressible bilayer structure, assuming $\bar{\mu} = 0$ henceforth.

Figure 6 displays the widely studied critical stretch λ_{cr} plotted against a broad range of film-to-substrate stiffness ratio of the bilayer structure, covering also the range for relatively more compliant films on substrates, for a fully compressible bilayer with $\nu_f = \nu_s = 0$ and a nearly incompressible bilayer with $\nu_f = \nu_s = 0.99$, with film thickness $h_f = 1$. Remember that the parameter $\bar{c}$ is the cohesive resistance against the separation of film and substrate. Hence, as $\bar{c} \to \infty$, our solutions here converge to the classical (perfectly bonded) bilayer case, as shown in Figure 6, where the curve for $\bar{c} = 10^6$ recovers the results presented in Bakiler et al. [29], with a clear flattening of the bifurcation curve at $E_f/E_s = 1$. The case of a classical bilayer structure therefore is essentially the lower most curve on the graphs. As the cohesive stiffness $\bar{c}$ decreases and approaches zero, we observe two behaviors. First, the flattening out of the

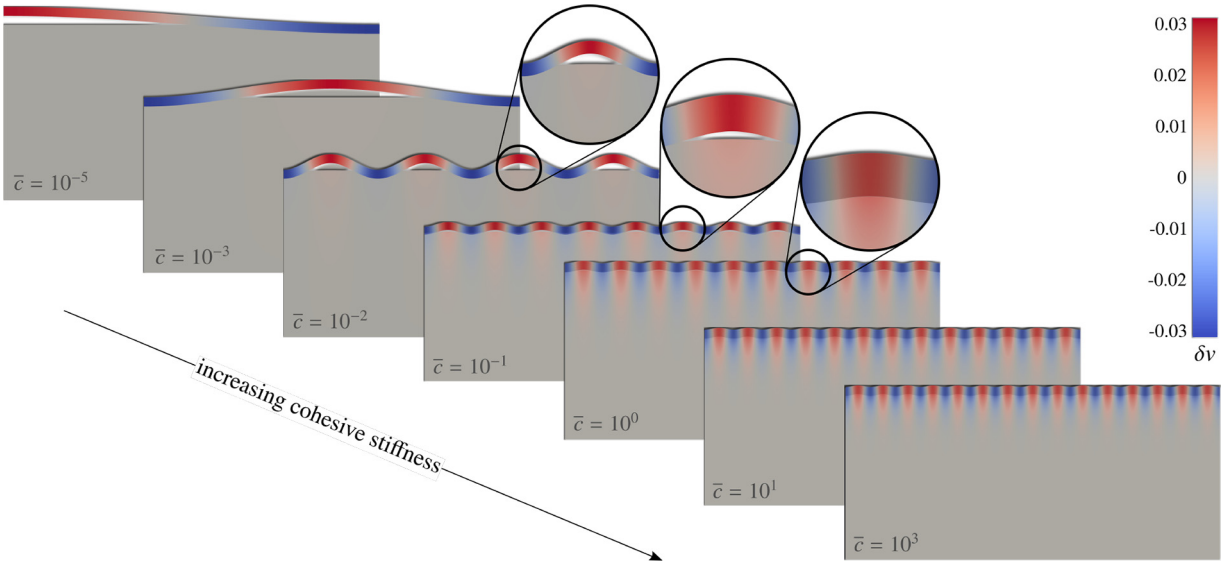

Figure 7. Deformation profiles for a bilayer structure with different cohesive stiffnesses, $h_f = 1$ and $\nu_f = \nu_s = 0$, obtained from FEM enhanced with eigenvalue analysis. Deformation profiles are portrayed by looking at the eigenvector corresponding to the first negative eigenvalue. Color scale maps incremental displacement in the γ direction.

bifurcation curve at and beyond $E_f/E_s = 1$ is still present, yet a transition region begins to form in between, which can be clearly seen. Second, the structure starts to buckle at increasing λ_{cr}, as we see the lines approaching a constant of $\lambda_{cr} = 1$. This happens because as $\bar{c} \to 0$, what we expect to see is complete delamination of the film from the substrate and hence for the film to behave as a beam. This can be explained better using the next illustration.

Figure 7 illustrates clearly the buckling behavior of the bilayer structure for several values of $\bar{c}$, via numerical results obtained from FEM enhanced with eigenvalue analysis. The deformation profiles given in Figure 7 are essentially the eigenvectors corresponding to the first negative eigenvalues of the system. Since an infinite half-space is impossible to realize, the substrate has been truncated at a suitable depth and horizontal roller supports have been placed at the bottom. The right and left sides are on vertical roller supports. Clearly, as $\bar{c} \to 0$, for instance at $\bar{c} = 10^{-5}$, the film is almost completely delaminated from the substrate and itself behaves as a beam. The half-wave mode observed in the beam here is due to the roller boundary conditions on the vertical axis. As the cohesive stiffness $\bar{c}$ increases, film delamination is still observed, however, to a lesser degree, accompanied by increasing wavenumbers. The coloring maps the incremental vertical displacements, and it can be seen that as cohesive stiffness increases and the film is bound more strongly to the substrate, the wrinkling of the film moves "further down" the substrate before it fully decays, as expected.

After observing the general trend of how critical stretch changes over a wide range of stiffness ratios in Figure 6 and with respect to changing cohesive stiffness, the surface graphs in Figure 8 illustrate this behavior for a continuous range of cohesive stiffnesses and for $E_f/E_s \geqslant 1$. One key aspect of this work is that the compressibility of the domains are kept as material parameters throughout. Hence, Figure 8 also illustrates the results for two different Poisson's ratios in each row, assuming film and substrate have the same Poisson's ratio, although the formulation allows for different Poisson's ratios also. Once again, the classical bilayer limit which is recovered with increasing $\bar{c}$ has been marked, and the point on this line where $E_f/E_s = 1$ indicates the well-known half-space limit, which renders $\lambda_{cr} = 0.486$ for a fully compressible half-space [27,28] and $\lambda_{cr} = 0.543$ for an almost incompressible half-space, recovering the findings of Biot [13]. The framework for a bilayer system with a general interface formulated here is hence shown to recover both the classical bilayer limit and the half-space solutions. Cohesive stiffness has a clear effect on critical stretch, more significant with decreasing stiffness ratio, and we see that the commonly accepted classical bilayer constitutes only a limit of the solution. Looking at the effect of

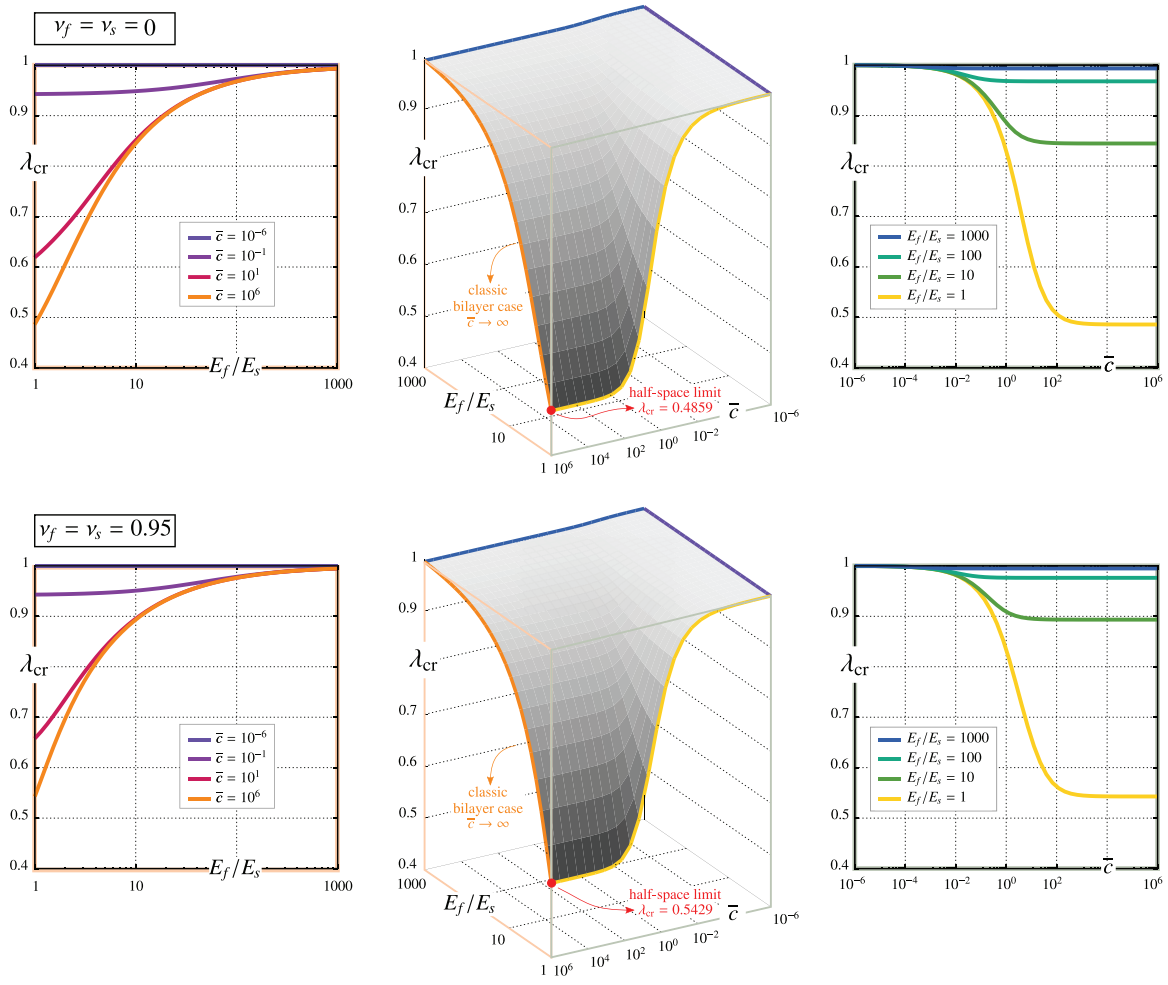

Figure 8. Surface graph (center) of critical stretch λ_{cr} versus E_f/E_s and $\bar{c}$, for two different compressibilities, $\nu_f = \nu_s = 0$ and $\nu_f = \nu_s = 0.95$. 2D insets show projections of λ_{cr} versus E_f/E_s for several values of $\bar{c}$ (left), and λ_{cr} versus $\bar{c}$ for several values of E_f/E_s (right), for $h_f = 1$.

compressibility, we see that a change in compressibility most influences the result for more stiff cohesive interfaces, which is also illustrated clearly in Figure 9.

Figure 9 plots the critical stretch λ_{cr} with respect to changing cohesive stiffness $\bar{c}$ and Poisson's ratio $\nu = \nu_f = \nu_s$. Clearly, the effect of changing cohesive stiffness increases significantly as we move from incompressibility at $\nu = 1$ toward a fully compressible system with $\nu = 0$. Once again, from the 2D insets on the left, we see that as cohesive stiffness decreases, the system becomes increasingly less dependent on changing Poisson's ratio, and the greatest effect of changing Poisson's ratio is observed in a system with $\bar{c} = 10^6$.

Figure 10 investigates further the effect of Poisson's ratio on the bifurcation behavior of a bilayer system, along changing the cohesive stiffness $\bar{c}$, where the film and substrate are no longer assumed to have the same Poisson's ratio. An interesting observation here is that changing film compressibility, that is, moving from column to column, has little effect on bifurcation point, whereas changing substrate compressibility, that is, looking among the three different colors of lines, has a significant effect on critical stretch. For stiffness ratio $E_f/E_s = 2$, shown in the top row, moving from a fully compressible substrate to an incompressible one influences an almost 17% change in critical stretch λ_{cr} for the higher cohesive stiffness regime. This trend is also observed for other stiffness ratios and for all film Poisson's ratios.

Next, we compare the numerical results obtained via FEM with their theoretical counterparts that have been presented thus far. Figures 11 and 12 display results for critical stretch λ_{cr} and critical

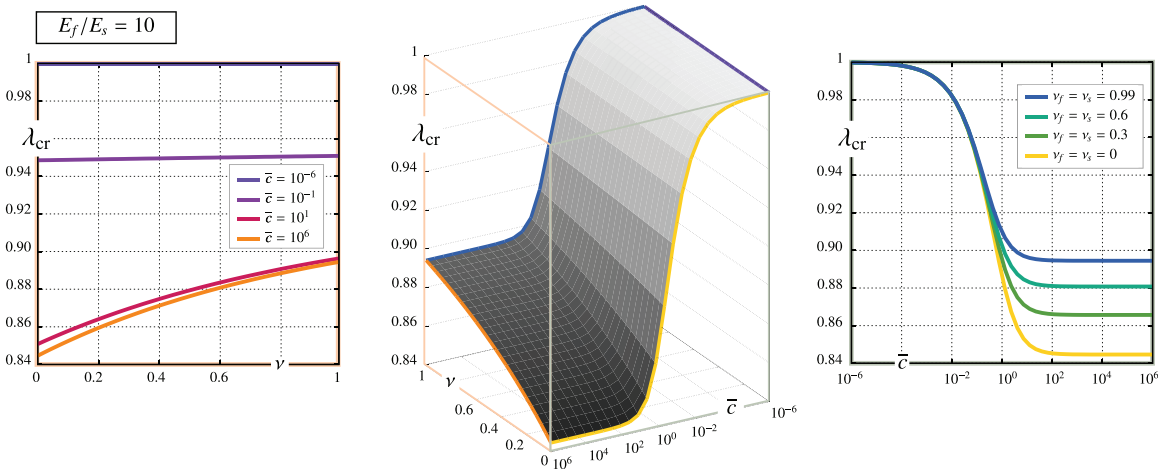

Figure 9. Surface graph (center) of critical stretch λ_{cr} versus $\nu = \nu_f = \nu_s$ and $\bar{c}$, for stiffness ratio $E_f/E_s = 10$. 2D insets show projections of λ_{cr} versus ν for several values of $\bar{c}$ (left), and λ_{cr} versus $\bar{c}$ for several values of ν (right), for $h_f = 1$.

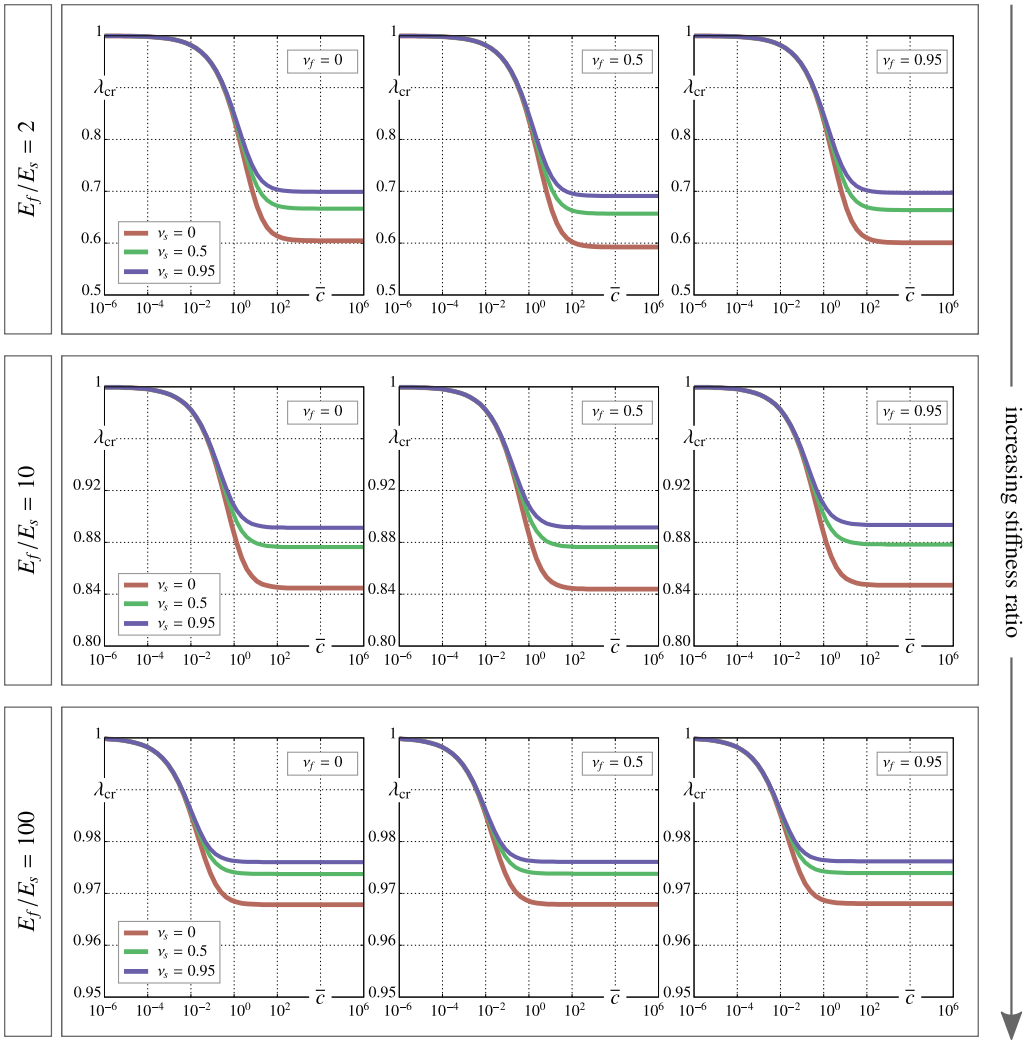

Figure 10. Critical stretch λ_{cr} versus cohesive stiffness $\bar{c}$, for different Poisson's ratio combinations for film and substrate, each row depicting a different stiffness ratio E_f/E_s, for $h_f = 1$.

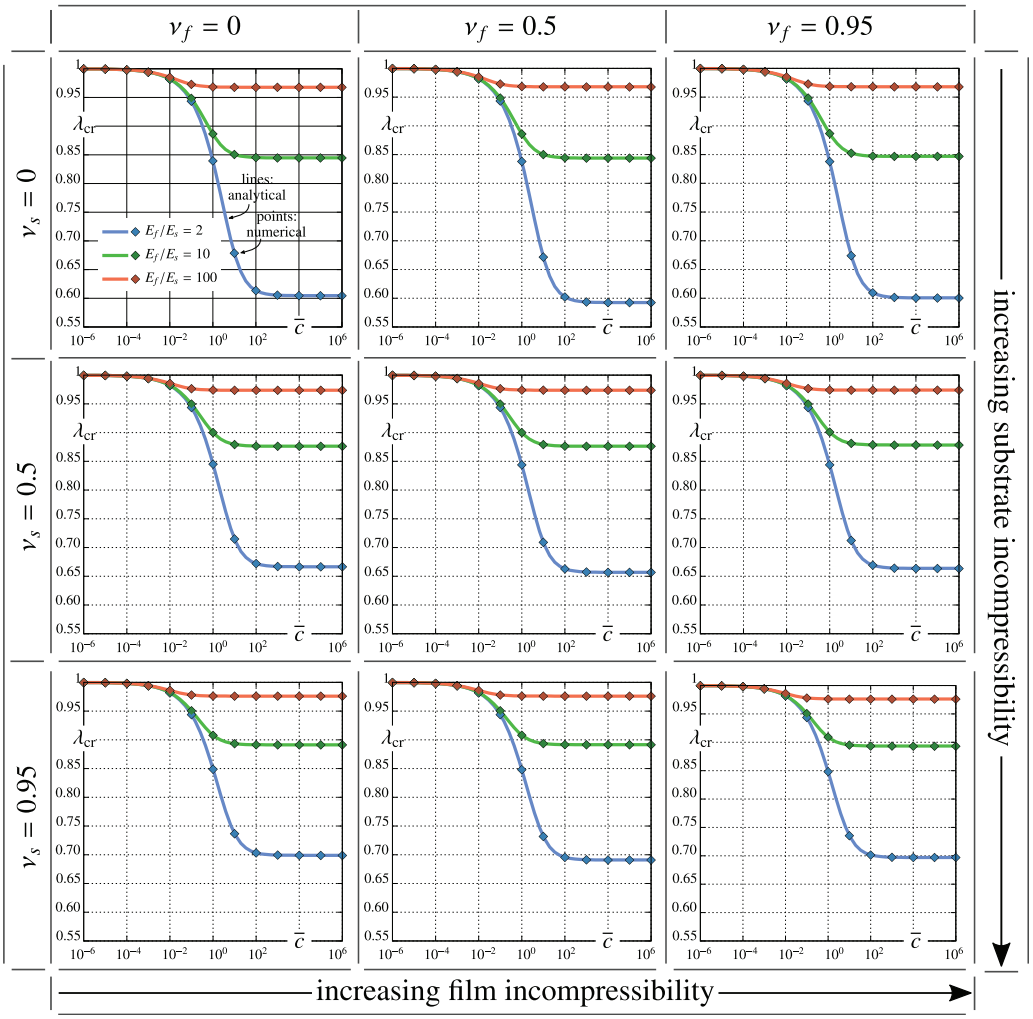

Figure 11. Critical stretch λ_{cr} versus $\bar{c}$ displayed together with numerical findings, shown as points, over a range of stiffness ratio and combinations of film and substrate Poisson's ratio, for $h_f = 1$.

wavenumber k_{cr}, respectively, with changing cohesive stiffness $\bar{c}$, for three different stiffness ratios in each inset, and each inset for a different combination of film and substrate Poisson's ratio. Once again, the influence of substrate and film compressibility on critical stretch and wavenumber can be seen here. For both critical stretch and critical wavenumber, an excellent agreement between the theoretical results and numerical findings is observed. An interesting observation stemming from Figure 12 is that the critical wavenumber converges to a different value for each stiffness ratio as $\bar{c}$ is increased, seen by the flattening and separation of the curves. On the other end of the cohesive stiffness spectrum, where the cohesive stiffness approaches zero, however, we see that stiffness ratio ceases to have any influence on critical wavenumber. This happens because with relatively low cohesive stiffness, the film is weakly bonded to the substrate; hence, we mostly observe "beam buckling" of the film, similar to delamination, and therefore, the stiffness of the film or the substrate no longer affects the bifurcation pattern.

Finally, we investigate the influence of film thickness on bifurcation behavior, shown in Figure 13. The critical stretch of a classical bilayer system is expected to be independent of film thickness, see, for example, Javili and Bakiler [80], among others. Here, we observe that the critical stretch becomes less dependent on film thickness *for increasing* $\bar{c}$; however, if the cohesive stiffness is not extremely high, we actually *see a significant dependence of the critical stretch* λ_{cr} *on the film thickness*. This behavior originates from the fact that in classical bilayers, there exists only one length scale, namely, the film thickness h, and thus, the wavelength becomes proportional to the film thickness such that the wavenumber k

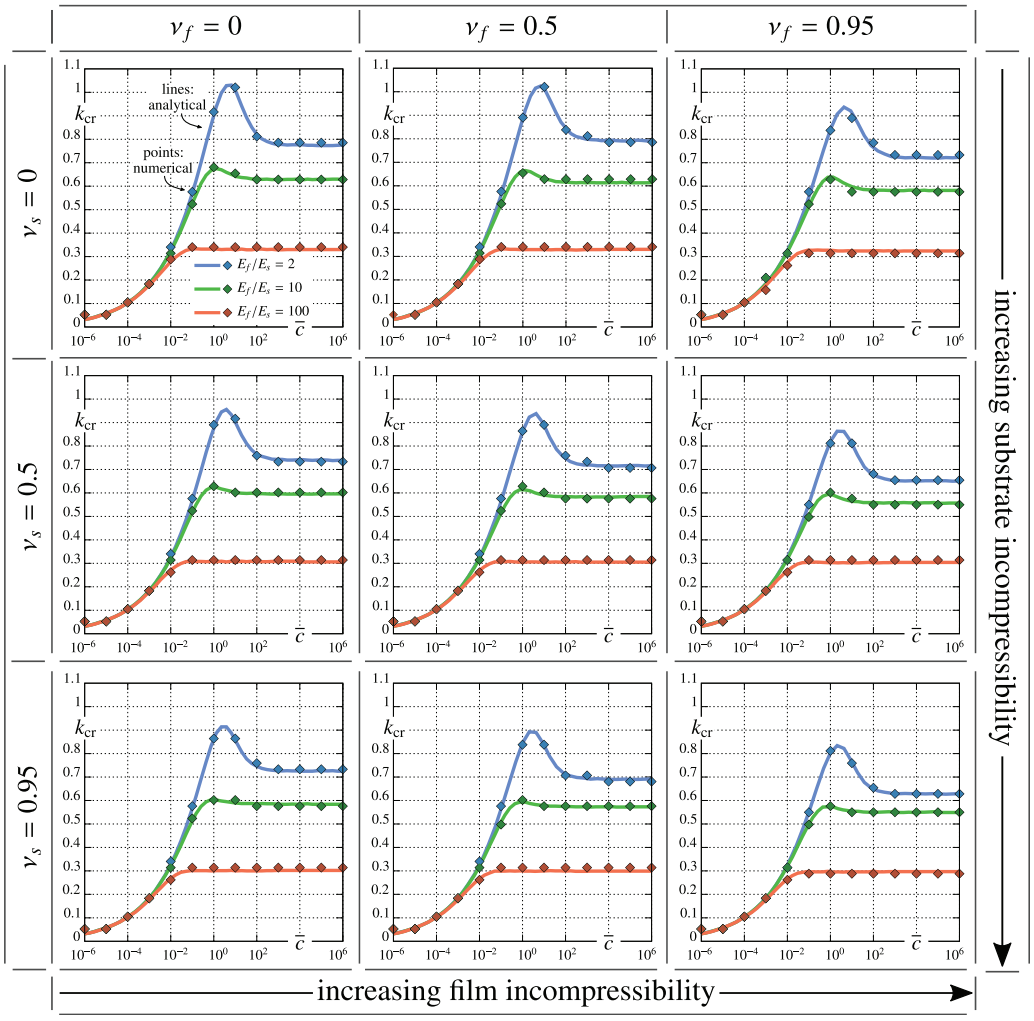

Figure 12. Critical wavelength k_{cr} versus $\bar{c}$ displayed together with numerical findings, shown as points, over a range of stiffness ratio and combinations of film and substrate Poisson's ratio, for $h_f = 1$.

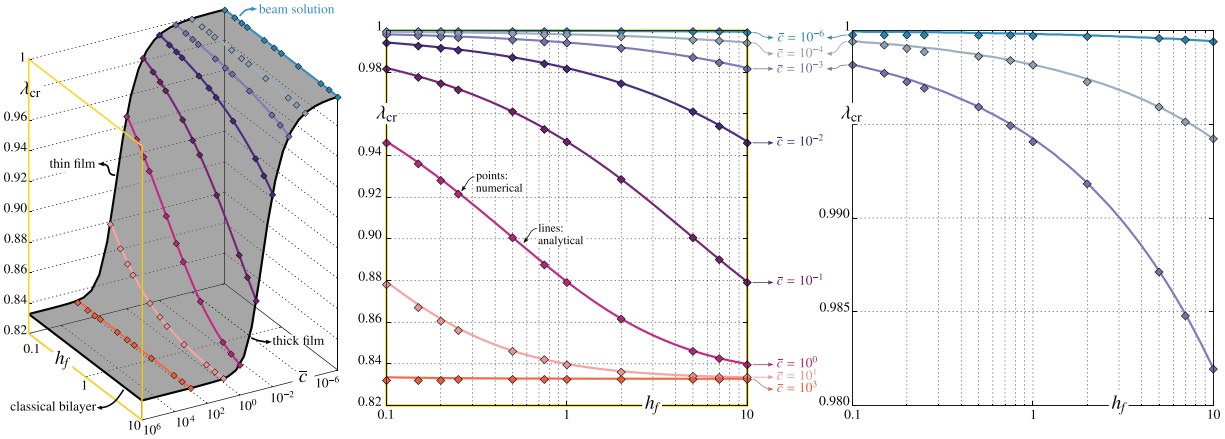

Figure 13. Critical stretch λ_{cr} versus film thickness h_f displayed together with numerical findings, shown as points, over a range of cohesive stiffness $\bar{c}$, for $E_f/E_s = 5$ and $\nu_f = \nu_s = 0.95$, as a continuous surface (left) and a 2D projection (center). The right inset displays an enlarged version of the upper range of the center inset.

multiplied by the film thickness kh becomes a dimensionless parameter characterizing the system. However, by incorporating an interface into the bilayer model and hence introducing cohesive stiffness to the system, another length scale $\mu/\bar{c}$ is introduced that influences the bifurcation behavior. More precisely, the wavenumber appears also in the dimensionless parameter $\mu k/\bar{c}$ (see, for instance, equation (66)). A continuous surface highlighting the change of bifurcation point with changing film thickness over a range of cohesive stiffness values is illustrated in Figure 13 (left).

6. Conclusion

In this manuscript, we have developed a generic framework accounting for the *general interface model* to capture the instability behavior of a *compressible* bilayer domain at large deformations. Furthermore, the utility of the framework to other geometries such as coated beams or half-spaces has been examined. The bifurcation behavior and its dependence on various parameters such as cohesive stiffness, stiffness ratio, film thickness, and most importantly compressibility has been thoroughly explored via the established theoretical framework but also compared with the accompanying numerical results, wherein an excellent agreement between the two has been observed. Our findings show that substrate compressibility together with cohesive stiffness have a significant effect on the overall bifurcation behavior of a bilayer system. Finally, although the bifurcation onset of classical bilayers is commonly accepted to be independent of film thickness, we show that this notion is merely one limit of a much broader spectrum when interface is accounted for. That is, the onset of bifurcation depends substantially on film thickness in the presence of a cohesive interface between the film and the substrate, due to the additional length scale introduced to the system, which is entirely absent in classical bilayers. This work provides grounds for further studies on how an interphase layer can be approximated via an interface model. One possible extension of this contribution is to enhance the general interface model to take into account the flexural resistance [73] in addition to elasticity along the interface and cohesive resistance across the interface.

Funding

The author(s) disclosed receipt of the following financial support for the research, authorship, and/or publication of this article: The authors gratefully acknowledge the support provided by the Scientific and Technological Research Council of Turkey (TÜBITAK) Career Development Program, grant number 218M700.

ORCID iD

Ali Javili https://orcid.org/0000-0001-7965-7088

References

[1] Budday, S, Kuhl, E, and Hutchinson, JW. Period-doubling and period-tripling in growing bilayered systems. *Philos Mag* 2015; 95: 3208–3224.
[2] Eskandari, M, Javili, A, and Kuhl, E. Elastosis during airway wall remodeling explains multiple co-existing instability patterns. *J Theor Biol* 2016; 403: 209–218.
[3] Cao, Y, and Hutchinson, JW. Wrinkling phenomena in neo-Hookean film/substrate bilayers. *ASME J Appl Mech* 2012; 79: 031019.
[4] Stafford, CM, Vogt, BD, Harrison, C, et al. Elastic moduli of ultrathin amorphous polymer films. *Macromolecules* 2006; 39: 5095–5099.
[5] Jia, Z, and Li, T. Effect of interfacial stiffness on the stretchability of metal/elastomer bilayers under in-plane biaxial tension. *Theor Appl Mech Lett* 2021; 11(3): 100247.
[6] Javili, A. Variational formulation of generalized interfaces for finite deformation elasticity. *Math Mech Solids* 2018; 23(9): 1303–1322.
[7] Budday, S, Steinmann, P, and Kuhl, E. The role of mechanics during brain development. *J Mech Phys Solids* 2014; 72: 75–92.
[8] Genzer, J, and Groenewold, J. Soft matter with hard skin: from skin wrinkles to templating and material characterization. *Soft Matter* 2006; 2: 310–323.
[9] Lejeune, E, Javili, A, Weickenmeier, J, et al. Tri-layer wrinkling as a mechanism for anchoring center initiation in the developing cerebellum. *Soft Matter* 2016; 12: 5613–5620.

[10] Harrison, C, Stafford, CM, Zhang, W, et al. Sinusoidal phase grating created by a tunably buckled surface. *Appl Phys Lett* 2004; 85: 4016–4018.
[11] Zhang, J, Li, Y, and Xing, Y. Theoretical and experimental investigations of transient thermo-mechanical analysis on flexible electronic devices. *Int J Mech Sci* 2019; 160: 192–199.
[12] Biot, M. Bending of an infinite beam on an elastic foundation. *J Appl Math Mech* 1937; 203: A-1–A-7.
[13] Biot, MA. Surface instability of rubber in compression. *Appl Sci Res A* 1961; 12: 168–182.
[14] Allen, HG. *Analysis and design of structural sandwich panels*. London: Pergamon Press, 1969.
[15] Andres, S, Steinmann, P, and Budday, S. The origin of compression influences geometric instabilities in bilayers. *Proc R Soc A* 2018; 474: 20180267.
[16] Cai, ZX, and Fu, YB. Effects of pre-stretch, compressibility and material constitution on the period-doubling secondary bifurcation of a film/substrate bilayer. *Int J Nonlin Mech* 2019; 115: 11–19.
[17] Goriely, A, and Ben Amar, M. Differential growth and instability in elastic shells. *Phys Rev Lett* 2005; 94: 198103.
[18] Javili, A, Dortdivanlioglu, B, Kuhl, E, et al. Computational aspects of growth-induced instabilities through eigenvalue analysis. *Comput Mech* 2015; 56: 405–420.
[19] Cao, Y, and Hutchinson, JW. From wrinkles to creases in elastomers: the instability and imperfection-sensitivity of wrinkling. *Proc R Soc A* 2012; 468: 94–115.
[20] Stoop, N, Lagrange, R, Terwagne, D, et al. Curvature-induced symmetry breaking determines elastic surface patterns. *Nat Mater* 2015; 14: 337–342.
[21] Zhuo, L, and Zhang, Y. From period-doubling to folding in stiff film/soft substrate system: the role of substrate nonlinearity. *Int J Nonlin Mech* 2015; 76: 1–7.
[22] Sozio, F, and Yavari, A. Nonlinear mechanics of surface growth for cylindrical and spherical elastic bodies. *J Mech Phys Solids* 2017; 98: 12–48.
[23] Li, B, Jia, F, Cao, YP, et al. Surface wrinkling patterns on a core-shell soft sphere. *Phys Rev Lett* 2011; 106: 234301.
[24] Zhang, C, Hao, YK, Li, B, et al. Wrinkling patterns in soft shells. *Soft Matter* 2018; 14: 1681–1688.
[25] Cao, YP, Jia, F, Zhao, Y, et al. Buckling and post-buckling of a stiff film resting on an elastic graded substrate. *Int J Solids Struct* 2012; 49: 1656–1664.
[26] Steigmann, DJ, and Ogden, RW. Plane deformations of elastic solids with intrinsic boundary elasticity. *Proc R Soc A* 1997; 453: 853–877.
[27] Murphy, J, and Destrade, M. Surface waves and surface stability for a pre-stretched, unconstrained, non-linearly elastic half-space. *Int J Nonlin Mech* 2009; 44: 545–551.
[28] Bakiler, AD, and Javili, A. Bifurcation behavior of compressible elastic half-space under plane deformations. *Int J Nonlin Mech* 2020; 126: 103553.
[29] Bakiler, AD, Dortdivanlioglu, B, and Javili, A. From beams to bilayers: a unifying approach towards instabilities of compressible domains under plane deformations. *Int J Nonlin Mech* 2021; 135: 103752.
[30] Firooz, S, Steinmann, P, and Javili, A. Homogenization of composites with extended general interfaces: comprehensive review and unified modeling. *Appl Mech Rev* 2021; 73(4): 040802.
[31] Lejeune, E, Javili, A, and Linder, C. Understanding geometric instabilities in thin films via a multi-layer model. *Soft Matter* 2016; 12: 806–816.
[32] Lejeune, E, Javili, A, and Linder, C. An algorithmic approach to multi-layer wrinkling. *Extreme Mech Lett* 2016; 7: 10–17.
[33] Wang, C, Zhang, S, Nie, S, et al. Buckling of a stiff thin film on a bi-layer compliant substrate of finite thickness. *Int J Solid Struct* 2020; 188–189: 133–140.
[34] Zhou, M, Cai, Z, and Fu, Y. Post-buckling of an elastic half-space coated by double layers. *Math Mech Solids* 2021; 27: 193–209.
[35] Bi, H, Wang, B, Su, C, et al. Buckling behaviour of a stiff thin film on a finite-thickness bi-layer substrate. *Int J Solid Struct* 2021; 219–220: 177–187.
[36] Asdaque, PM, Banerjee, S, and Roy, S. An electromechanically coupled intrinsic, mixed variational formulation for geometrically nonlinear smart composite beam. *Appl Math Model* 2019; 65: 549–565.
[37] Kim, DH, Kim, YS, Wu, J, et al. Ultrathin silicon circuits with strain-isolation layers and mesh layouts for high-performance electronics on fabric, vinyl, leather, and paper. *Adv Mater* 2009; 21: 3703–3707.
[38] Bigoni, D, Bordignon, N, Piccolroaz, A, et al. Bifurcation of elastic solids with sliding interfaces. *Proc R Soc A* 2018; 474: 20170681.
[39] Huy, HP, and Sanchez-Palencia, E. Phénomènes de transmission à travers des couches minces de conductivitéélevée. *J Math Anal Appl* 1974; 47(2): 284–309.
[40] Sanchez-Palencia, E. Comportements local et macroscopique d'un type de milieux physiques heterogenes. *Int J Eng Sci* 1974; 12(4): 331–351.
[41] Hashin, Z. Thermoelastic properties of particulate composites with imperfect interface. *J Mech Phys Solids* 1991; 39(6): 745–762.
[42] Benveniste, Y, and Miloh, T. Imperfect soft and stiff interfaces in two-dimensional elasticity. *Mech Mater* 2001; 33(6): 309–323.

[43] Fried, E. Correspondence between a phase-field theory and a sharp-interface theory for crystal growth. *Contin Mech Thermodyn* 1997; 9: 33–60.
[44] Mei, H, Landis, CM, and Huang, R. Concomitant wrinkling and buckle-delamination of elastic thin films on compliant substrates. *Mech Mater* 2011; 43: 627–642.
[45] Hu, KM, Liu, YQ, Zhou, LW, et al. Delamination-free functional graphene surface by multiscale, conformal wrinkling. *Adv Fun Mater* 2020; 30(34): 1–11.
[46] Xuan, Y, Guo, X, Cui, Y, et al. Crack-free controlled wrinkling of a bilayer film with a gradient interface. *Soft Matter* 2012; 8(37): 9603–9609.
[47] Vella, D, Bico, J, Boudaoud, A, et al. The macroscopic delamination of thin films from elastic substrates. *Proc Natl Acad Sci USA* 2009; 106(27): 10901–10906.
[48] Sun, Y, Choi, WM, Jiang, H, et al. Controlled buckling of semiconductor nanoribbons for stretchable electronics. *Nat Nanotechnol* 2006; 1: 201–207.
[49] Li, J, Slesarenko, V, and Rudykh, S. Microscopic instabilities and elastic wave propagation in finitely deformed laminates with compressible hyperelastic phases. *Eur J Mech A Solid* 2019; 73: 126–136.
[50] Pocivavsek, L, Pugar, J, O'Dea, R, et al. Topography-driven surface renewal. *Nat Phys* 2018; 14(9): 948–953.
[51] Daher, N, and Maugin, GA. The method of virtual power in continuum mechanics application to media presenting singular surfaces and interfaces. *Acta Mech* 1986; 60(3–4): 217–240.
[52] Barenblatt, GI. The formation of equilibrium cracks during brittle fracture General ideas and hypotheses. Axially-symmetric cracks. *J Appl Math Mech* 1959; 23(3): 622–636.
[53] Barenblatt, GI. The mathematical theory of equilibrium cracks in brittle fracture. *Adv Appl Mech* 1962; 7: 55–129.
[54] Dugdale, D. Yielding of steel sheets containing slits. *J Mech Phys Solids* 1960; 8(2): 100–104.
[55] Wei, Y, and Hutchinson, JW. *Interface strength, work of adhesion and plasticity in the peel test*. Dordrecht: Springer 1998, pp. 315–333.
[56] Alfano, G, and Crisfield, MA. Finite element interface models for the delamination analysis of laminated composites: mechanical and computational issues. *Int J Num Method Eng* 2001; 50(7): 1701–1736.
[57] Van, Den, Bosch, MJ, Schreurs, PJ, and Geers, MG. On the development of a 3D cohesive zone element in the presence of large deformations. *Comput Mech* 2008; 42(2): 171–180.
[58] Reinoso, J, Paggi, M, and Blázquez, A. A nonlinear finite thickness cohesive interface element for modeling delamination in fibre-reinforced composite laminates. *Compos Part B: Eng* 2017; 109: 116–128.
[59] Brassart, L, Inglis, HM, Delannay, L, et al. An extended Mori-Tanaka homogenization scheme for finite strain modeling of debonding in particle-reinforced elastomers. *Comput Mater Sci* 2009; 45(3): 611–616.
[60] Fagerström, M, and Larsson, R. Theory and numerics for finite deformation fracture modelling using strong discontinuities. *Int J Num Method Eng* 2006; 66(6): 911–948.
[61] Park, K, Paulino, GH, and Roesler, JR. A unified potential-based cohesive model of mixed-mode fracture. *J Mech Phys Solids* 2009; 57(6): 891–908.
[62] Xu, XP, and Needleman, A. Numerical simulations of fast crack growth in brittle solids. *J Mech Phys Solids* 1994; 42(9): 1397–1434.
[63] Ortiz, M, and Pandolfi, A. Finite-deformation irreversible cohesive elements for three-dimensional crack-propagation analysis. *Int J Num Method Eng* 1999; 44(9): 1267–1282.
[64] Charlotte, M, Laverne, J, and Marigo, JJ. Initiation of cracks with cohesive force models: a variational approach. *Eur J Mech A Solid* 2006; 25(4): 649–669.
[65] Kawashita, LF, and Hallett, SR. A crack tip tracking algorithm for cohesive interface element analysis of fatigue delamination propagation in composite materials. *Int J Solid Struct* 2012; 49(21): 2898–2913.
[66] Gasser, TC, and Holzapfel, GA. Geometrically non-linear and consistently linearized embedded strong discontinuity models for 3D problems with an application to the dissection analysis of soft biological tissues. *Comput Meth Appl Mech Eng* 2003; 192(47–48): 5059–5098.
[67] Mergheim, J, and Steinmann, P. A geometrically nonlinear FE approach for the simulation of strong and weak discontinuities. *Comput Meth Appl Mech Eng* 2006; 195(37–40): 5037–5052.
[68] Chen, T, Chiu, MS, and Weng, CN. Derivation of the generalized Young-Laplace equation of curved interfaces in nanoscaled solids. *J Appl Phys* 2006; 100(7): 074308.
[69] Javili, A, Mcbride, A, and Steinmann, P. Thermomechanics of solids with lower-dimensional energetics: on the importance of surface, interface, and curve structures at the nanoscale. A unifying review. *Appl Mech Rev* 2013; 65: 010802.
[70] Gurtin, ME, and Murdoch, AI. A continuum theory of elastic material surfaces. *Arch Ration Mech Anal* 1975; 57: 291–323.
[71] Moeckel, GP. Thermodynamics of an interface. *Arch Ration Mech Anal* 1975; 57(3): 255–280.
[72] Fried, E, and Gurtin, ME. Thermomechanics of the interface between a body and its environment. *Contin Mech Thermodyn* 2007; 19(5): 253–271.
[73] Steigmann, DJ, and Ogden, RW. Elastic surface–substrate interactions. *Proc R Soc A* 1999; 455: 437–474.

[74] Fried, E, and Todres, RE. Mind the gap: the shape of the free surface of a rubber-like material in proximity to a rigid contactor. *J Elast* 2005; 80(1–3): 97–151.
[75] Hashin, Z. Thin interphase/imperfect interface in elasticity with application to coated fiber composites. *J Mech Phys Solids* 2002; 50(12): 2509–2537.
[76] Monchiet, V, and Bonnet, G. Interfacial models in viscoplastic composites materials. *Int J Eng Sci* 2010; 48(12): 1762–1768.
[77] Benveniste, Y. Models of thin interphases with variable moduli in plane-strain elasticity. *Math Mech Solids* 2013; 18(2): 119–134.
[78] Javili, A, Steinmann, P, and Mosler, J. Micro-to-macro transition accounting for general imperfect interfaces. *Comput Meth Appl Mech Eng* 2017; 317: 274–317.
[79] Ogden, RW. Large deformation isotropic elasticity—on the correlation of theory and experiment for incompressible rubberlike solids. *Proc R Soc Lond A* 1972; 328: 567–583.
[80] Javili, A, and Bakiler, AD. A displacement-based approach to geometric instabilities of a film on a substrate. *Math Mech Solids* 2019; 24: 2999–3023.